A ductile phase-field model based on degrading the fracture toughness: Theory and implementation at small strain

Bo Yin, Michael Kaliske[*]

Institute for Structural Analysis, TU Dresden, 01187, Germany

Abstract

A reliable prediction of structural failure is extremely important in industrial applications. The promising phase-field model has been intensively studied in fracture simulation and been validated by experiments to effectively predict crack initiation, propagation as well as branching. Experimentally motivated, a variety of phase-field models have been proposed for ductile fracture, which redefine either the fracture driving force $\mathcal{H}$ consisting of both the elastic energy and the pseudo plastic energy or modify the degradation function $g(d)$ of the fracture driving force $\mathcal{H}$. Different from the existing approaches, this work formulates a novel ductile phase-field model by defining the fracture toughness $\mathcal{G}_c$ depending on the accumulated plastic strain, i.e. the local fracture toughness decreases due to increased plastic deformation. The phase-field driving force $\mathcal{H}$ is still defined only consisting of the elastic strain potential based on the definition of GRIFFITH-type fracture. As a result, the locally increasing $\mathcal{H}$ and the locally decreasing $\mathcal{G}_c$ govern the ductile fracture evolution simultaneously. This approach is formulated for small strain by coupling the classical VON MISES plasticity and, subsequently, is implemented into the context of the Finite Element (FE) framework. Several representative examples are evaluated to demonstrate the capabilities of the model, and corresponding findings and perspectives are consequently summarized.
© 2020 Elsevier B.V. All rights reserved.

1. Introduction

Fracture is one of the most crucial failure mechanisms in industrial engineering and the reliable prediction of crack initiation and propagation is of great importance. Generally, structural failure is the result of either microscopic debonding between atoms or molecules, or macroscopic separation of material components. Brittle fracture usually occurs at relatively small deformation and leads to an abrupt loss of strength by fast and unstable crack growth. The underlying physical concept is outlined firstly by GRIFFITH [1], that the generation of a new crack surface inside materials requires a specific amount of energy within the whole solid. As the source of this energy, GRIFFITH proposed the strain energy potential stored in the solid during its deformation, i.e. the stored strain potential energy is irreversibly dissipated to form crack surfaces. The measurement of the amount of energy to create a unit crack surface is defined as the critical energy release rate or fracture toughness $\mathcal{G}_c$, which is considered as a material

---

0045-7825/© 2020 Elsevier B.V. All rights reserved.

constant. Unlike brittle fracture, ductile fracture is associated with hardening or necking phenomena before fracture. Since plastic deformation is permanent and irreversible, a portion of internal energy is dissipated by the inelastic properties, which leads to fracture occurring at relatively large deformation. Motivated by experimental findings, pioneers have developed several numerical models to describe plastic behavior as well as material failure criteria, see e.g. [2–4] for an overview.

A number of computational models have been proposed to couple classical plasticity to continuum damage mechanics depending on concepts of irreversible deformation and softening of material strength properties. One of the simplest approaches investigates the local initiation of fracture by employing a damage variable, which is independent of plastic deformation, see [5]. Meanwhile, a coupled formulation by linking the evolution of damage and plasticity is further developed, see e.g. [6–16] particularly for isotropic damage and [17] for anisotropic damage. Furthermore, the plasticity-damage formulation is extended to the microplane framework, which is an unconventional but efficient technique. The fundamental constitutive theory is outlined in [18] and, subsequently, is applied to concrete structures, see e.g. [19,20].

Besides classical continuum damage models, the promising phase-field model based on GRIFFITH-type fracture can effectively simulate material failure as well. Unlike the material force method [21–26] and the cohesive zone approach [27], the phase-field approach is a smeared and diffusive approximation of sharp cracks, which is proposed by FRANCFORT & MARIGO to minimize the total energy by a variational principle, see [28]. It is subsequently regularized by BOURDIN et al. [29] to formulate the classical GRIFFITH-type fracture, also see [30–32]. To enhance the reliability of the phase-field method for fracture simulation, classical Γ-convergence theory has been studied in [33–38]. Another key feature for a trustworthy crack evolution is the definition of the fracture driving force. AMOR et al. [39] propose an energy split based on the volumetric–deviatoric decomposition, while MIEHE et al. [40] defines the driving force based on a spectral split principle, also see [41]. A recent split accounting for the crack's orientation to define the driving stress is proposed in [42] for small strain. Furthermore, another approach named representative crack element (RCE) [43] is developed by incorporating homogenization concept to physically describe the crack kinematics.

Incorporating phase-field modeling, ductile fracture has been studied recently. Based on a virtual-power formulation, [44] formulates ductile fracture evolution in elasto-plastic materials by introducing two independent variables, namely the phase-field and the accumulated plastic strain, with appropriate constraints considering irreversibility. An alternative approach redefines the phase-field driving force consisting of both the elastic energy and the pseudo plastic energy, see [45,46], that achieves a transition from brittle to ductile fracture. Based on this idea, stress triaxiality has been investigated in [47] by scaling the contribution of the plastic energy to the fracture evolution. A recent work [48] also studies ductile failure of frictional soil materials undergoing large deformations. Additionally, a theoretical study of the combination of brittle, cohesive and ductile fracture is reported in [49] by evaluating a representative one-dimensional problem. To get rid of the mesh-dependency of classical plasticity, a gradient-extended ductile phase-field model [50–52] is developed based on micromorphic regularization, that employs two additional degrees of freedom, namely the phase-field and the non-local hardening variable, to govern fracture and plasticity evolution, respectively. Moreover, since classical VON MISES plasticity is unable to capture volumetric plastic deformation properly, [53] extends the ductile phase-field model towards finite plasticity by accounting for the volumetric yielding response. The property of void nucleation and coalescence is subsequently studied in [54]. In addition to redefining the driving force, [55] develops a ductile fracture model at small strain by modifying the degradation function depending on the plastic hardening state. Nevertheless, the crack driving force of this approach only consists of the elastic strain energy, which yields a different ductile failure mechanism compared to the ones aforementioned. In the sequel, this ductile phase-field model is successfully extended to finite strain and is validated experimentally in [56]. Comprehensively, a recent review highlighted in [57] compares these existing ductile phase-field models qualitatively.

In this work, a new ductile fracture mechanism is proposed by defining the fracture toughness depending on the accumulated plastic deformation. In addition to the phase-field degradation function $g(d)$ multiplying by the driving force, a degradation function f is introduced to decrease the fracture toughness $\mathcal{G}_c$ along with the increase of the plastic deformation. This approach is motivated by fatigue phase-field modeling [58–60] and strain rate-dependent fracture [61]. Furthermore, the driving force is defined to only consist of the elastic strain potential using the volumetric–deviatoric split, which is similar to [55,56]. As a result, the overall ductile fracture evolution is governed by the locally increased elastic strain energy and the locally degraded $\mathcal{G}_c$ simultaneously. With the
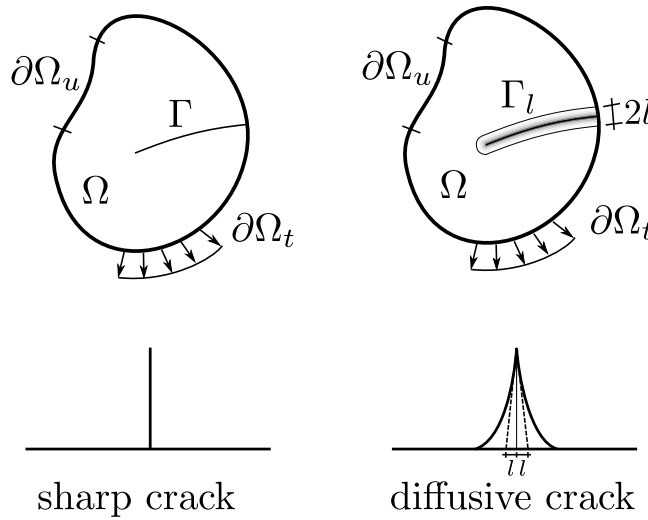
Fig. 1. Diffusive crack topology.

above conceptual understanding, the presented ductile phase-field evolution is formulated by incorporating classical VON MISES plasticity. Meanwhile, several assumptions are considered, that largely simplify the derivation and implementation. The priority of this paper is to evaluate the reasonableness of the presented methodology and to demonstrate the capability of its numerical applications.

The framework of this paper is outlined as follows. In Section 2, the fundamentals of the ductile phase-field formulation, the concept of hardening dependent fracture toughness as well as the governing equations are introduced. In Section 3, the algorithmic setups regarding classical VON MISES plasticity and numerical implementation are highlighted. Subsequently, a couple of representative numerical examples are given in Section 4. Section 5 summarizes the findings and closes the paper with potential perspectives.

2. Ductile phase-field evolution

2.1. Phase-field topology

Within a continuous solid domain, a sharp crack is numerically approximated by a diffusive phase-field distribution, see Fig. 1. A scalar parameter, namely the phase-field variable $d(\boldsymbol{x}, t)$, is introduced to identify the material state, i.e. the undamaged material is denoted by $d = 0$ and the fully cracked state is represented by $d = 1$. Motivated by a one-dimensional bar with an infinite length $L \in [-\infty, +\infty]$, which is assumed to have a crack at position $x = 0$, the closed form solution for a continuous phase-field according to [31] is approximated by an exponential function

$$d(x) = \exp(-\frac{|x|}{l}), \tag{1}$$

which is naturally bounded by $(0 < d \leq 1)$. The length scale parameter l is employed to govern the width of the transition zone between fractured and unfractured states. Extending to a two- or three-dimensional framework, the second order functional of the crack surface density yields

$$\gamma_l = \frac{1}{2l} \left(d^2 + l^2 |\nabla d|^2 \right), \tag{2}$$

where $\nabla (*)$ denotes the spatial gradient operator. Highlighted in [38], the realistic crack length Γ is approximately obtained by the phase-field crack length Γ_l as long as $l \to 0$, i.e.

$$\Gamma \approx \lim_{l \to 0} \Gamma_l = \lim_{l \to 0} \int_{\Omega} \gamma_l \, dV, \tag{3}$$

which is known as the classical Γ-convergence condition for fracture.

The defined crack surface density function in Eq. (2) is known as the AT2 model, which yields an exponentially-shaped crack profile as described by Eq. (1). By applying this function, the numerical derivation and implementation are quite straightforward and efficient without additional numerical treatment due to the differentiable (except for $d = 0$) and continuous properties of the phase-field solution in Eq. (1). Nevertheless, this model does not present an elastic limit and the simulation result largely depends on the length scale parameter l. As [41] investigated with respect to FEM application, a minimum element size $h_e \leq l/2$ in the potential crack region is necessary in order to achieve realistic results.

Meanwhile, another common alternative for the crack surface density function is the classical AT1 model, which only consists of the linear term d rather than the quadratic term d^2 in Eq. (2), see [32]. The AT1 model can guarantee an ideally linear elastic response up to the elastic stress limit. However, due to the lack of differential continuity, specific numerical treatment is of importance to avoid negative phase-field values, which may lead to a non-linear phase-field evolution. In this contribution, for simplicity, ductile fracture evolution is formulated based on the AT2 model.

2.2. HELMHOLTZ *energy density function*

The phase-field model for brittle fracture is based on a variational principle, see [28], and has subsequently been regularized in [29]. In this paper, ductile fracture evolution based on the phase-field framework is proposed. The elasto-plastic constitutive formulation of the material property is derived within the small strain framework. The total HELMHOLTZ energy Φ of the system is defined as

$$\Phi = \int_{\Omega} \left(\left(g\left(d\right) \varphi_e^+ + \varphi_e^- \right) + \varphi_p \right) dV + \Phi_c, \tag{4}$$

where the elastic strain energy density contains two parts, i.e. the fracture driving part φ_e^+ and the non-driving part φ_e^-. Only the fracture driving part is degraded by the function $g(d)$ to evolve the phase-field. The degradation function $g\left(d\right)$ in Eq. (4) should satisfy the fundamental mathematical properties

$$g\left(0\right) = 1, \quad g\left(1\right) = 0, \quad \partial_d\, g\left(d\right) \geq 0 \quad \text{and} \quad \partial_d\, g\left(1\right) = 0, \tag{5}$$

where the first two conditions in Eq. (5) indicate the bounds of the unbroken and fully broken states, respectively. The other two conditions in Eq. (5) prescribe a monotonic degradation during the fracture evolution procedure. An early proposal in [29] gives a simple quadratic function as

$$g\left(d\right) = \left(1 - d\right)^2. \tag{6}$$

Subsequently, several alternative options have been studied, e.g. in [42,61–64], as well.

Regarding the fracture driving force, two common splits are postulated, namely the volumetric–deviatoric split [39] and the spectral split [40]. Recently, two other alternatives are formulated in [42,43] to obtain realistic crack kinematics by modifying the material constitutive relation, which are nevertheless restricted to small strain so far. In this work, to be consistent with classical J_2-plasticity, the volumetric–deviatoric split is applied for the ductile phase-field evolution. The crack driving and non-driving energy terms are defined as

$$\varphi_e^+ = \frac{1}{2}\kappa \langle I_1 \rangle_+^2 + \mu \left(\boldsymbol{\varepsilon}_{e,dev} : \boldsymbol{\varepsilon}_{e,dev} \right) \quad \text{and} \quad \varphi_e^- = \frac{1}{2}\kappa \langle I_1 \rangle_-^2, \tag{7}$$

respectively. Here, κ and μ are two model parameters regarding the elastic properties. The quantity I_1 in Eq. (7) represents the first invariant of the elastic strain tensor $\boldsymbol{\varepsilon}_e$, which is obtained by $\boldsymbol{\varepsilon}_e = \boldsymbol{\varepsilon} - \boldsymbol{\varepsilon}_p$. The plastic strain tensor $\boldsymbol{\varepsilon}_p$ is an internal variable. The deviatoric part of the elastic strain tensor is obtained by $\boldsymbol{\varepsilon}_{e,dev} = \boldsymbol{\varepsilon}_e - \frac{1}{3} I_1 \mathbf{1}$, where $\mathbf{1}$ represents the second order identity tensor. The operator $\langle * \rangle_{\pm}$ is defined as a selective operator $\langle * \rangle_{\pm} = \frac{1}{2} \left(* \pm | * | \right)$. By using this split, the volumetric energy does not evolve the crack as long as the material is compressed.

Furthermore, a linear isotropic hardening law for the plasticity evolution is considered in this work and the plastic energy density function φ_p in Eq. (4) is defined as

$$\varphi_p = \sigma_y\, \alpha + \frac{1}{2}\, H\, \alpha^2, \tag{8}$$

where the critical yield stress σ_y and the hardening modulus H are two key material constants to govern plasticity evolution. In this work, only the non-softening situation, which characterizes the hardening modulus $H \geq 0$, is taken into consideration. The internal variable α represents the hardening state. The evolutions of the hardening variable α and the plastic strain $\boldsymbol{\varepsilon}_p$ are discussed in Section 3.1.

The last term Φ_c in Eq. (4), namely the energy required to generate crack surfaces, is approximated by

$$\Phi_c \approx \mathcal{G}_c \, \Gamma_l = \mathcal{G}_c \int_\Omega \gamma_l \, dV, \tag{9}$$

where $\mathcal{G}_c$ is known as the critical energy release rate or the fracture toughness for the fracture evolution. It is defined as the critical value of the strain energy release within an infinitesimal crack length, see [1]. For brittle phase-field modeling, this quantity is characterized as a material parameter, which is constant and independent of the loading state. Nevertheless, in this work, this quantity $\mathcal{G}_c$ is assumed to be non-constant and evaluated depending upon the plastic deformation. Thus, a ductile fracture model is postulated by incorporating the phase-field model as well as the plastic evolution.

2.3. Hardening dependent fracture toughness $\mathcal{G}_c$

To extend the classical brittle phase-field modeling to a ductile phase-field approach, the material resistance is assumed to be affected by the accumulated plastic deformation. In this formulation, a degraded fracture toughness $\mathcal{G}_c$ due to the evolution of plasticity is proposed for ductile phase-field modeling. Similar applications are found in [58–60] for fatigue phase-field analysis and in [61] for strain rate-dependent fracture study. The fracture toughness $\mathcal{G}_c$ is defined as

$$\mathcal{G}_c = f\left(\zeta\left(t\right)\right) \cdot \mathcal{G}_c^0, \tag{10}$$

where $\mathcal{G}_c^0$ is a material constant representing fracture toughness for brittle fracture. Particularly, f is a function of an internal variable ζ and is called hardening degradation function. It is characterized by the following properties

$$0 < f \leq 1, \quad f\left(\zeta \leq \zeta^{cr}\right) = 1, \quad \text{and} \quad \partial_\zeta f\left(\zeta \geq \zeta^{cr}\right) \leq 0. \tag{11}$$

The first condition in Eq. (11) indicates a physical bound of f, i.e. the fracture toughness $\mathcal{G}_c$ in Eq. (10) cannot exceed $\mathcal{G}_c^0$ and cannot be an unphysically negative value. The second condition introduces an internal variable threshold ζ^{cr} to control when the degradation is triggered. The last one prescribes a monotonic decrease of $\mathcal{G}_c$, when $\zeta \geq \zeta^{cr}$. These pre-conditions in Eq. (11) postulate a physical and reasonable conceptual understanding of the ductile fracture mechanism of the presented phase-field formulation. Certainly, several alternative functional forms can be chosen to construct the hardening degradation function. In this work, a general and simple form

$$f\left(\zeta\right) = \begin{cases} 1, & \zeta < \zeta_{cr}, \\ \frac{1-b}{a^2}\left(\zeta - \zeta_{cr} - a\right)^2 + b, & \zeta_{cr} \leq \zeta < a + \zeta_{cr}, \\ b, & \zeta \leq a + \zeta_{cr}, \end{cases} \tag{12}$$

is applied. Specifically, a and b are two key parameters to control the profile of the degradation function f, see Fig. 2. The parameter b is characterized as the lower bound of $f\left(\zeta\right)$, which is restricted as $0 < b \leq 1$. Nevertheless, in order to have an effective reduction of $f\left(\zeta\right)$, the parameter b in this work is particularly set as an infinitesimal value $0 < b \ll 1$. An important reason for this is that fracture will be fully evolved when the fracture toughness $\mathcal{G}_c$ is degraded to a certain level, which is far away from 0. Moreover, an infinitesimal value of b can largely enhance the numerical stability when solving the phase-field equilibrium at the fully cracked state compared to the case $b = 0$.

It is noteworthy to mention that, due to the special non-linearity of $f(\zeta)$, the differentiation of f with respect to the internal variable ζ does not generally exist, except for the special case of $\zeta_{cr} = 0$. Therefore, an important assumption of

$$\frac{\partial f\left(\zeta\right)}{\partial \zeta} = 0 \tag{13}$$

is proposed, which largely simplifies the derivation work. To support this assumption, several numerical treatments can be employed. For instance, within an infinitesimal time increment, f is numerically obtained by the history
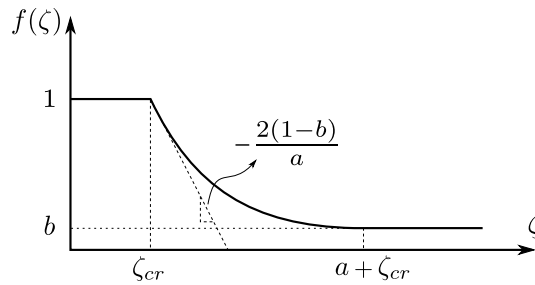
Fig. 2. The profile of the hardening degradation function $f(\zeta)$.

variable ζ^n at previous step t^n rather than ζ^{n+1} at current step t^{n+1}, which leads to the differentiation of f regarding the current ζ^{n+1} vanishing, i.e. $\partial f(\zeta^n)/\partial \zeta^{n+1} = 0$.

Regarding the definition of the internal variable ζ, various alternative options can be employed. In this work, motivated by [55], classical VON MISES equivalent plastic strain

$$\zeta = \sqrt{\frac{2}{3}} \int_0^t \sqrt{\dot{\boldsymbol{\varepsilon}}^p : \dot{\boldsymbol{\varepsilon}}^p} \, dt \tag{14}$$

is used. Thus, $\zeta \geq 0$ naturally exists.

2.4. Governing equations of ductile fracture

In this section, a constitutive evolution for ductile phase-field modeling for a quasi-static case is developed. For simplification, the proof of thermodynamic consistency is not presented in this work, which is nevertheless referred, e.g. to [2,51,55]. Without considering the body force and the surface traction, the governing equation of the mechanical response reads

$$\nabla \cdot \boldsymbol{\sigma} = \mathbf{0}, \tag{15}$$

where the total stress tensor is composed by $\boldsymbol{\sigma} = g(d)\,\boldsymbol{\sigma}^+ + \boldsymbol{\sigma}^-$. The positive and negative stresses are obtained by $\boldsymbol{\sigma}^\pm = \partial \varphi_e^\pm / \partial \boldsymbol{\varepsilon}_e$. The material is assumed to exhibit associative J_2-plasticity with linear isotropic hardening and the yield surface function $\mathcal{F}$ reads

$$\mathcal{F} = \|\boldsymbol{\sigma}_{dev}\| - \sqrt{\frac{2}{3}} t_\alpha, \tag{16}$$

where the first term represents the norm of the degraded deviatoric stress tensor $\boldsymbol{\sigma}_{dev} = \boldsymbol{\sigma} - \frac{1}{3} tr(\boldsymbol{\sigma})\,\mathbf{1}$. The quantity t_α is known as the plasticity thermodynamic force and is obtained as

$$t_\alpha = \frac{\partial \varphi_p}{\partial \alpha} = \sigma_y + H \cdot \alpha. \tag{17}$$

Due to associative properties, the evolution equations for the plastic strain $\boldsymbol{\varepsilon}_p$ as well as the hardening variable α are defined as

$$\dot{\boldsymbol{\varepsilon}}_p = \dot{\chi} \frac{\partial \mathcal{F}}{\partial \boldsymbol{\sigma}} \qquad \text{and} \qquad \dot{\alpha} = \dot{\chi} \frac{\partial \mathcal{F}}{\partial t_\alpha}, \tag{18}$$

respectively. The factor $\dot{\chi}$ is known as the plastic multiplier. The second order tensor $\partial \mathcal{F}/\partial \boldsymbol{\sigma}$ describes the plastic flow direction. The KUHN–TUCKER conditions

$$\dot{\chi} \geq 0, \qquad \mathcal{F} \leq 0 \qquad \text{and} \qquad \mathcal{F} \cdot \dot{\chi} = 0 \tag{19}$$

always exist when the material is in the elastic domain or the plastic domain. The algorithmic setup of the elasto-plastic evolution is discussed in Section 3.1.

Furthermore, the governing equation for the ductile phase-field model is obtained based on the internal power $\dot{\Phi}$ with respect to $\dot{d}$, which yields

$$
\begin{aligned}
\partial_d \Phi \cdot \dot{d} &= \int_\Omega \left(\partial_d\, g\,(d)\, \varphi_e^+ \cdot \dot{d} + f\,(\zeta)\, \mathcal{G}_c^0 \Big((\partial_d\, \gamma_l)\, \dot{d} + (\partial_{\nabla d}\, \gamma_l)\, \nabla \dot{d} \Big) \right) dV \\
&= \int_\Omega \left(\partial_d\, g\,(d)\, \varphi_e^+ \cdot \dot{d} + f\,(\zeta)\, \mathcal{G}_c^0\, \frac{d}{l}\, \dot{d} + \mathcal{G}_c^0\, l\, f\,(\zeta)\, \nabla d \cdot \nabla \dot{d} \right) dV.
\end{aligned}
\tag{20}
$$

Since the degradation function $f\,(\zeta)$ depends on the internal variable ζ and is characterized as non-constant, the gradient of the degradation cannot be neglected, i.e. $\nabla f\,(\zeta) \neq \mathbf{0}$. Therefore, the term $\left(f\,(\zeta) \cdot \nabla d \cdot \nabla \dot{d} \right)$ in Eq. (20) is obtained as

$$
f\,(\zeta) \cdot \nabla d \cdot \nabla \dot{d} = \nabla \left(f\,(\zeta)\, \nabla d \cdot \dot{d} \right) - \nabla f\,(\zeta) \cdot \nabla d \cdot \dot{d} - f\,(\zeta) \cdot \Delta d \cdot \dot{d},
\tag{21}
$$

where the LAPLACIAN operator is denoted by $\Delta\,(*)$. Substituting Eq. (21) into Eq. (20) yields

$$
\begin{aligned}
\partial_d \Phi \cdot \dot{d} &= \int_\Omega \left(\left(\partial_d\, g\,(d)\, \varphi_e^+ + \mathcal{G}_c^0 \left(f\, \frac{d}{l} - l\, \nabla f \cdot \nabla d - l\, f \cdot \Delta d \right) \right) \dot{d} + \mathcal{G}_c^0\, l\, \nabla \Big(f\, \nabla d \cdot \dot{d} \Big) \right) dV \\
&= \int_\Omega \left(\partial_d\, g\,(d)\, \varphi_e^+ + \mathcal{G}_c^0 \left(f\, \frac{d}{l} - l\, \nabla f \cdot \nabla d - l\, f \cdot \Delta d \right) \right) \dot{d}\, dV + \int_{\partial \Omega} \mathcal{G}_c^0\, l\, \Big(f\, \nabla d \cdot \dot{d} \Big) \cdot \mathbf{n}\, dA.
\end{aligned}
\tag{22}
$$

The unit normal vector outwards at the solid surface is denoted by $\mathbf{n}$. Neglecting the surface integration terms in Eq. (22), the governing equation for ductile phase-field evolution reads

$$
- \partial_d\, g\,(d)\, \varphi_e^+ + \mathcal{G}_c^0 \cdot \left(f\,(\zeta)\, l\, \Delta d + l\, \nabla f\,(\zeta) \cdot \nabla d - f\,(\zeta)\, \frac{d}{l} \right) = 0.
\tag{23}
$$

Several recent contributions [58–60] have presented similar strong forms of the phase-field equation, nevertheless, in the field of fatigue fracture.

In order to avoid healing of the phase-field, the driving force φ_e^+ in Eq. (25) is alternatively substituted by an additional internal quantity

$$
\mathcal{H} = \underset{0 \leq \tau \leq t^{n+1}}{\mathrm{Max}}\, \varphi_e^+\,(\boldsymbol{\varepsilon}_e, \tau)
\tag{24}
$$

to achieve a damage-like irreversible phase-field evolution, see [40]. As a result, the consequent governing equation for the phase-field is rewritten as

$$
- \partial_d\, g\,(d)\, \mathcal{H} + \mathcal{G}_c^0 \cdot \left(f\,(\zeta)\, l\, \Delta d + l\, \nabla f\,(\zeta) \cdot \nabla d - f\,(\zeta)\, \frac{d}{l} \right) = 0.
\tag{25}
$$

3. Algorithmic setup

3.1. Plasticity evolution

With respect to the simplicity of the VON MISES yield function, classical radial return mapping is applied to evolve the internal hardening variables, see [2]. The plastic flow direction at t^{n+1} in Eq. (18) is a unit vector normal to the VON MISES yield surface, which reads

$$
\mathbf{\mathcal{N}}^{n+1} = \frac{\partial \mathcal{F}}{\partial \boldsymbol{\sigma}^{n+1}} = \frac{\boldsymbol{\sigma}_{dev}^{n+1}}{\| \boldsymbol{\sigma}_{dev}^{n+1} \|}.
\tag{26}
$$

Within a pseudo-time increment $[t^n, t^{n+1}]$, the internal variables are generally expressed as

$$
\boldsymbol{\varepsilon}_p^{n+1} = \boldsymbol{\varepsilon}_p^n + \Delta \chi\, \mathbf{\mathcal{N}}^{n+1} \qquad \text{and} \qquad \alpha^{n+1} = \alpha^n + \sqrt{\frac{2}{3}}\, \Delta \chi.
\tag{27}
$$

The key is to find the proper internal variables to satisfy the KUHN–TUCKER conditions consistently

$$
\Delta \chi \geq 0, \qquad \mathcal{F}^{n+1} \leq 0 \qquad \text{and} \qquad \mathcal{F}^{n+1} \cdot \Delta \chi = 0.
\tag{28}
$$

Outlined in [2], the yield function in the trial state is checked to examine if the material response is in the pure elastic domain or the elastic–plastic domain. The deviatoric stress tensor for the trial state is computed as

$$\boldsymbol{\sigma}_{dev}^{n+1,tr} = g\,(d)\,2\mu\,\boldsymbol{\varepsilon}_{e,dev}^{n+1,tr} = g\,(d)\,2\mu\,\left(\boldsymbol{\varepsilon}_{dev}^{n+1} - \boldsymbol{\varepsilon}_{p}^{n}\right). \tag{29}$$

It is necessary to point out that the plastic strain tensor $\boldsymbol{\varepsilon}_p$ is a natural deviatoric tensor in this case, i.e. $tr(\boldsymbol{\varepsilon}_p) = 0$. Another noteworthy point is that the plastic flow direction defined in Eq. (26) can be obtained by the stress tensor $\boldsymbol{\sigma}_{dev}^{n+1,tr}$ in the trial state as well, which yields

$$\mathcal{N}^{n+1} = \frac{\boldsymbol{\sigma}_{dev}^{n+1}}{\|\boldsymbol{\sigma}_{dev}^{n+1}\|} = \frac{\boldsymbol{\sigma}_{dev}^{n+1,tr}}{\|\boldsymbol{\sigma}_{dev}^{n+1,tr}\|}. \tag{30}$$

Neglecting proofs, the relation $\|\boldsymbol{\sigma}_{dev}^{n+1}\| = \|\boldsymbol{\sigma}_{dev}^{n+1,tr}\| - g\,(d)\,2\,\mu\,\Delta\chi$ also exists, see [55]. Furthermore, the hardening variable in the trial state is simply taken from the previous step, i.e. $\alpha^{n+1,tr} = \alpha^n$. Giving the deviatoric stress tensor and the hardening variable for the trial state, the trial yield function

$$\mathcal{F}^{n+1,tr} = \|\boldsymbol{\sigma}_{dev}^{n+1,tr}\| - \sqrt{\frac{2}{3}}\left(\sigma_y + H\cdot\alpha^{n+1,tr}\right) \tag{31}$$

is obtained. If $\mathcal{F}^{n+1,tr} \leq 0$, the current response is in pure elastic domain and the trial evaluation is the solution. Nevertheless, if $\mathcal{F}^{n+1,tr} > 0$, the evaluation at the trial state is not admissible and a plastic corrector step is necessary to achieve the conditions in Eq. (28). A common approach to obtain the solution is applying a local NEWTON procedure. Due to the special characteristics of the presented yield function, a closed-form solution of the plastic multiplier $\Delta\chi$ can be obtained by

$$\Delta\chi = \frac{\mathcal{F}^{n+1,tr}}{g\,(d)\,2\,\mu + \frac{2}{3}\cdot H}. \tag{32}$$

In the sequel, the internal variables $\boldsymbol{\varepsilon}_p^{n+1}$ and α^{n+1} are updated according to Eq. (27). This classical predictor and corrector algorithm is referred to [2] for a detailed description.

3.2. Stress and tangent moduli

After updating the internal variables, the explicit deviatoric stress tensor at the current step is computed by

$$\boldsymbol{\sigma}_{dev}^{n+1} = g\,(d)\,2\mu\,\left(\boldsymbol{\varepsilon}_{dev}^{n+1} - \boldsymbol{\varepsilon}_{p}^{n+1}\right) = \boldsymbol{\sigma}_{dev}^{n+1,tr} - g\,(d)\,2\mu\,\Delta\chi\,\mathcal{N}^{n+1}. \tag{33}$$

The consistent elasto-plastic tangent is derived as

$$\mathbb{C}_{dev}^{n+1} = \frac{\partial\,\boldsymbol{\sigma}_{dev}^{n+1}}{\partial\,\boldsymbol{\varepsilon}^{n+1}} = \frac{\partial\,\boldsymbol{\sigma}_{dev}^{n+1,tr}}{\partial\,\boldsymbol{\varepsilon}^{n+1}} - g\,(d)\,2\mu\,\left(\frac{\partial\,\Delta\chi}{\partial\,\boldsymbol{\varepsilon}^{n+1}}\otimes\mathcal{N}^{n+1} + \Delta\chi\cdot\frac{\partial\,\mathcal{N}^{n+1}}{\partial\,\boldsymbol{\varepsilon}^{n+1}}\right). \tag{34}$$

According to [2], the terms

$$\frac{\partial\,\Delta\chi}{\partial\,\boldsymbol{\varepsilon}^{n+1}} = \vartheta_1\,\mathcal{N}^{n+1} \qquad \text{with} \qquad \vartheta_1 = \frac{g\,(d)\,3\,\mu}{g\,(d)\,3\,\mu + H} \tag{35}$$

and

$$\frac{\partial\,\mathcal{N}^{n+1}}{\partial\,\boldsymbol{\varepsilon}^{n+1}} = \vartheta_2\,\left(\mathbb{P} - \mathcal{N}^{n+1}\otimes\mathcal{N}^{n+1}\right) \qquad \text{with} \qquad \vartheta_2 = \frac{g\,(d)\,2\,\mu}{\|\boldsymbol{\sigma}_{dev}^{n+1,tr}\|}, \tag{36}$$

are determined. Hence, the consequent deviatoric tangent is simplified as

$$\mathbb{C}_{dev}^{n+1} = g\,(d)\,2\mu\left((1 - \vartheta_2\,\Delta\chi)\,\mathbb{P} + (\vartheta_2\,\Delta\chi - \vartheta_1)\,\mathcal{N}^{n+1}\otimes\mathcal{N}^{n+1}\right), \tag{37}$$

where the index definition of the fourth order deviatoric tensor is $\mathbb{P}_{ijkl} = \frac{1}{2}\left(\delta_{ik}\delta_{jl} + \delta_{il}\delta_{jk}\right) - \frac{1}{3}\delta_{ij}\delta_{kl}$. Finally, based on the volumetric–deviatoric split, the elasto-plastic stress response and the consistent material tangent are

$$\boldsymbol{\sigma}^{n+1} = \kappa\left(g\,(d)\,\langle I_1^{n+1}\rangle_+ + \langle I_1^{n+1}\rangle_-\right)\mathbf{1} + \boldsymbol{\sigma}_{dev}^{n+1} \tag{38}$$

and

$$\mathbb{C}^{n+1} = \kappa \left(g\,(d)\,[I_1^{n+1}]_+ + [I_1^{n+1}]_- \right) \mathbf{1} \otimes \mathbf{1} + \mathbb{C}_{dev}^{n+1}, \tag{39}$$

respectively, where the operator $[*]_\pm = \partial \langle * \rangle_\pm / \partial *$ is defined.

3.3. Solution algorithm

Knowing the total elasto-plastic stress and tangent terms, the element residual and stiffness can be formed in the context of an FE application. According to the strong forms in Eqs. (15) and (25), the weak forms are easily obtained by multiplying virtual field quantities, e.g. $\delta\boldsymbol{u}$ and δd, with a subsequent volumetric integration, which are

$$\int_\Omega \left\{ \nabla \cdot \boldsymbol{\sigma}^{n+1} \cdot \delta\boldsymbol{u} \right\} dV = \int_{\partial\Omega} \left\{ \boldsymbol{\sigma}^{n+1} \cdot \boldsymbol{n} \cdot \delta\boldsymbol{u} \right\} dA - \int_\Omega \left\{ \boldsymbol{\sigma}^{n+1} : \nabla\delta\boldsymbol{u} \right\} dV. \tag{40}$$

and

$$\int_\Omega \left\{ -\partial_d\,g\,(d)\,\mathcal{H} + \mathcal{G}_c^0 \left(f\,(\zeta)\,l\,\Delta d + l\,\nabla f\,(\zeta) \cdot \nabla d - f\,(\zeta)\frac{d}{l} \right) \right\} \delta d\,dV = $$
$$- \int_\Omega \left\{ \partial_d\,g\,(d)\,\mathcal{H}\,\delta d + f\,(\zeta)\,\mathcal{G}_c^0 \left(\frac{d\,\delta d}{l} + l\,\nabla d \cdot \nabla\delta d \right) \right\} dV + \int_{\partial\Omega} \left\{ \mathcal{G}_c^0\,f\,(\zeta)\,l\,\nabla d \cdot \delta d \cdot \boldsymbol{n} \right\} dA. \tag{41}$$

For simplification, the surface integration terms in Eqs. (40) and (41) are not taken into consideration regarding FE implementation. Based on the concept of isoparametric interpolation, shape functions N^I are introduced to approximate $\boldsymbol{u}$, $\delta\boldsymbol{u}$ and d, δd from all the nodal values $\boldsymbol{u}^I$, $\delta\boldsymbol{u}^I$ and d^I, δd^I

$$\boldsymbol{u} = \sum_{I=1}^{n} N^I \boldsymbol{u}^I, \quad \delta\boldsymbol{u} = \sum_{I=1}^{n} N^I \delta\boldsymbol{u}^I, \quad d = \sum_{I=1}^{n} N^I d^I \quad \text{and} \quad \delta d = \sum_{I=1}^{n} N^I \delta d^I, \tag{42}$$

where the index n represents the number of nodes in one element. The index forms of the residuals and tangents for both the mechanical response and the phase-field evolution read

$$\boldsymbol{R}_{u_a}^I = -\int_\Omega \left\{ \sigma_{ac}^{n+1} \nabla_{x_c} N^I \right\} dV,$$

$$\boldsymbol{R}_d^I = -\int_\Omega \left\{ \left(\partial_d\,g(d)\,\mathcal{H} + \frac{f\,(\zeta)\,\mathcal{G}_c^0}{l}\,d \right) N^I + f\,(\zeta)\,\mathcal{G}_c^0\,l\,\nabla_{x_a} N^I \nabla_{x_a} d \right\} dV,$$

$$\boldsymbol{K}_{u_a u_b}^{IJ} = -\frac{\partial \boldsymbol{R}_{u_a}^I}{\partial \boldsymbol{u}_b^J} = \int_\Omega \left\{ \nabla_{x_c} N^I\,\mathbb{C}_{acbd}^{n+1}\,\nabla_{x_d} N^J \right\} dV, \tag{43}$$

$$\boldsymbol{K}_{dd}^{IJ} = -\frac{\partial \boldsymbol{R}_d^I}{\partial d^J} = \int_\Omega \left\{ \left(\partial_d^2\,g(d)\,\mathcal{H} + \frac{f\,(\zeta)\,\mathcal{G}_c^0}{l} \right) N^I N^J + f\,(\zeta)\,\mathcal{G}_c^0\,l\,\nabla_{x_a} N^I \nabla_{x_a} N^J \right\} dV,$$

respectively. For a staggered solution scheme, it is not necessary to have coupling terms between the mechanical field and the phase-field, since they are solved independently. In this work, the staggered scheme is applied to all numerical simulations and the solution process is outlined in [55].

4. Representative simulations

4.1. Uniaxial tension

Motivated by BORDEN et al. [47], this example studies ductile fracture of a uniaxial tension test to demonstrate the capability of the presented constitutive phase-field modeling. A single 8-node cubic linear element with the size of 1 m is subjected to uniaxial displacements monotonically. The model parameters are listed in Table 1. The threshold of the degradation function $f(\zeta)$ is set to $\zeta_{cr} = 0$, which indicates that $\mathcal{G}_c$ starts to decrease as soon as the material response is in the elasto-plastic domain. Several scaling factors a are tested to investigate ductile fracture behavior.

On the one hand, considering the material as an elasto-plastic solid, the evolution of the effective stress σ regarding the total strain ε for various a is shown in Fig. 3(a). At the beginning, up to reaching the yield stress, only

Table 1
Model parameters for the uniaxial tension test.

Bulk modulus κ	67 450 MPa	Critical value ζ_{cr}	0
Shear modulus μ	25 865 MPa	Factor b	$1 \cdot e^{-8}$
Hardening modulus H	655 MPa	Fracture toughness $\mathcal{G}_c^0$	138 J/mm^2
Yielding stress σ_y	320 MPa	Length scale l	2 m

(a) stress–strain relations for various a

(b) evaluation of $\mathcal{H}$ and $\mathcal{G}_c$ for $a = 1$
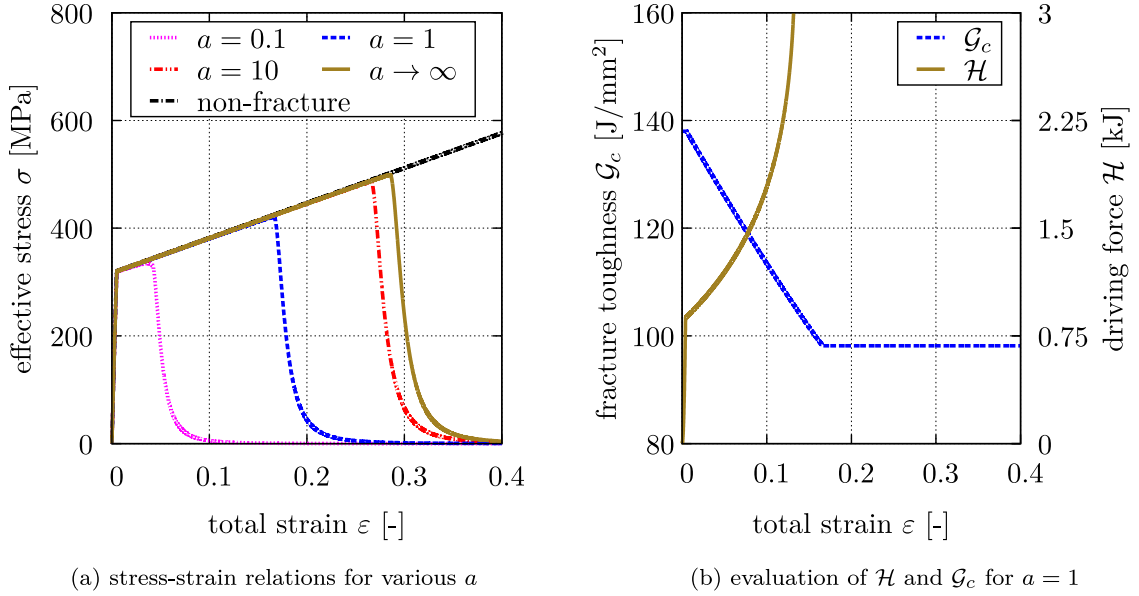
Fig. 3. Fracture evaluation of an elasto-plastic solid with the hardening modulus $H = 655$ MPa, (a) comparison of the stress–strain relationship for different scaling factors a and (b) evaluation of the driving force $\mathcal{H}$ and the fracture toughness $\mathcal{G}_c$ for $a = 1$.

the elastic response leads to a constant fracture toughness, i.e. $\mathcal{G}_c = \mathcal{G}_c^0$. Therefore, this procedure is characterized as a standard brittle phase-field evolution. Nevertheless, the fracture driving force $\mathcal{H}$ during the elastic deformation is significantly small to evolve the phase-field to $d = 1$. In the sequel, the constitutive law exhibits elasto-plastic properties when the effective stress exceeds the yield stress. Meanwhile, the ductile phase-field model is activated for the subsequent fracture evolution. In this case, the fracture mechanisms are governed by two aspects, e.g. an increase of the driving force $\mathcal{H}$ and a decrease of the fracture toughness $\mathcal{G}_c$. These two quantities are particularly measured with respect to the total strain ε by applying $a = 1$, see Fig. 3(b).

On the other hand, fracture evolution regarding perfect-plasticity is also evaluated, see Fig. 4(a). In this case, the elastic energy does not increase in the perfect-plastic domain due to perfect-plasticity. Thus, the driving force $\mathcal{H}$ nearly remains constant during the pure plastic deformation, which cannot evolve the phase-field to $d = 1$ immediately. Nevertheless, the accumulated plastic strain results in a gradual reduction of $\mathcal{G}_c$, which mainly governs the fracture up to the consequent rupture. Therefore, compared to the case of elasto-plasticity, the ductile fracture mechanism is slightly different by evaluating the evolutions of $\mathcal{H}$ and $\mathcal{G}_c$, see Fig. 4(b). It is noteworthy that, as a result of the transition phase-field value ($0 < d < 1$), a slightly increased $\mathcal{H}$ before the complete rupture is observed as well.

As aforementioned, the factor a governs the profile of the degradation function f, i.e. a larger value of a leads to less degraded $\mathcal{G}_c$ at the same plastic deformation. Hence, decreasing a eventually results in the ductile failure at comparatively small deformations, see Figs. 3(a) and 4(a). However, applying the value of a extremely close to ζ_{cr} may lead to several stability issues from the numerical point of view, since a slightly increased ζ with respect to ζ_{cr} yields an abrupt decrease of $\mathcal{G}_c$. Hence, reasonable and appropriate model parameters for ductile fracture are of great importance for the simulations. Furthermore, a nearly constant fracture toughness ($\mathcal{G}_c \approx \mathcal{G}_c^0$) is recovered by applying $a \to \infty$, and the response of the presented model for such a case completely agrees with the result stated in [47] with the hardening modulus $H = 655$ MPa.
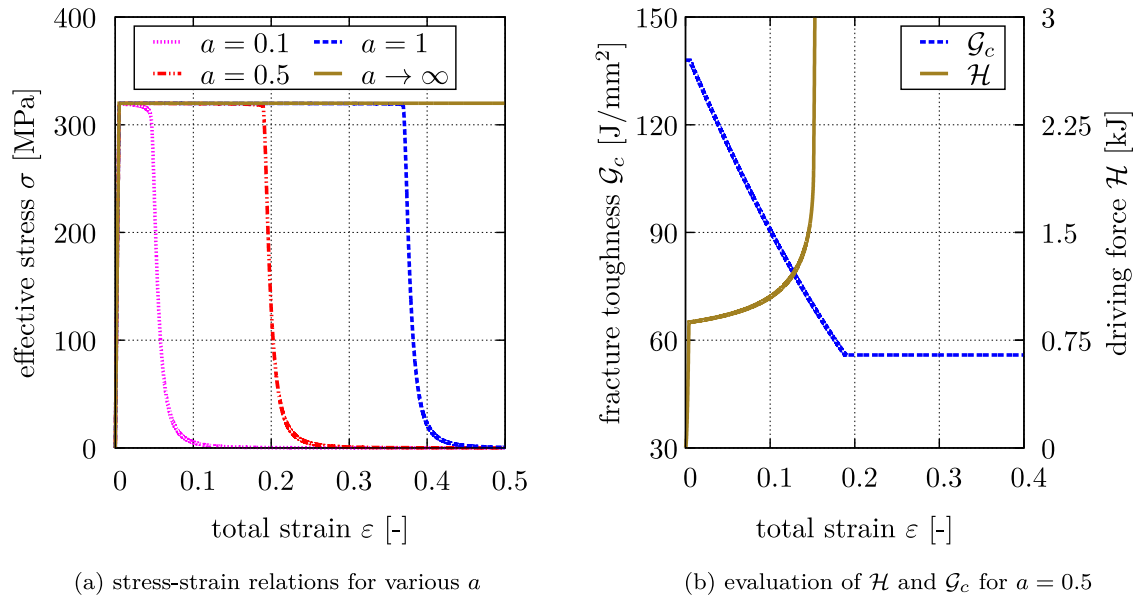
(a) stress-strain relations for various a

(b) evaluation of $\mathcal{H}$ and $\mathcal{G}_c$ for $a = 0.5$

Fig. 4. Fracture evaluation of a perfect-plastic solid ($H = 0$ MPa), (a) comparison of the stress–strain relationship for different scaling factors a and (b) evaluation of the driving force $\mathcal{H}$ and the fracture toughness $\mathcal{G}_c$ for $a = 0.5$.

Table 2
Model parameters for the symmetrically notched specimens.

Bulk modulus κ	71 666 MPa	Fracture toughness $\mathcal{G}_c^0$	$93.1 \cdot e^3$ kJ/m^2
Shear modulus μ	27 280 MPa	Critical value ζ_{cr}	0.001
Hardening modulus H	250 MPa	Factor a	0.2
Yielding stress σ_y	345 MPa	Factor b	$1 \cdot e^{-4}$
length scale l	2 mm		

Furthermore, motivated by [58–60], a cyclic load test based on the setup of elasto-plasticity ($H = 655$ MPa) is performed as well. The scaling factor is given by $a = 1.0$, which leads to material softening at approximately $\varepsilon = 0.17$ by applying a monotonic tension load, see Fig. 3(a). The cyclic loading function is given in Fig. 5(a), which consists of three full load cycles and a consequent monotonic load. The amplitude of the tensile displacement is given by $u_{max} = 0.0316$ m for the first three cycles, since this value is large enough to reach the elasto-plasticity but does not reach ductile failure yet. The effective stress regarding the total strain is shown in Fig. 5(b), that includes both tensile and compressive elasto-plasticity simultaneously. Observed in Fig. 5(c), the accumulative equivalent plastic strain ζ and the phase-field variable d present a stepwise increment simultaneously up to the material softening around $t = 6.8$ s and $\varepsilon = 0.022$. Meanwhile, the phase-field variable d is rapidly increasing from 0.2 to 1, nevertheless, the equivalent plastic strain ζ keeps more or less constant at $\zeta = 0.12$ up to the final failure.

4.2. Tension and compression fracture of a two-dimensional i-shaped specimen

Motivated by several previous works, see [48,55,65] to name a few, this example studies the phase-field crack propagation in an I-shaped specimen subjected to tension and compression load. The two-dimensional boundary value problem is depicted in Fig. 6(a), which is discretized by three different FE models consisting of 1248, 2144 and 5148 4-node quadratic elements for coarse, medium and fine meshes, respectively. The uniform element sizes at the slender part of the I-shaped specimen are $h_e = 1$ mm, $h_e = 0.75$ mm and $h_e = 0.5$ mm for these three meshes, see Fig. 6(b). The model parameters are listed in Table 2. According to the findings in [41], the reliability of the phase-field model in FE applications is guaranteed due to the given length scale parameter $l \geq 2h_e$ for all
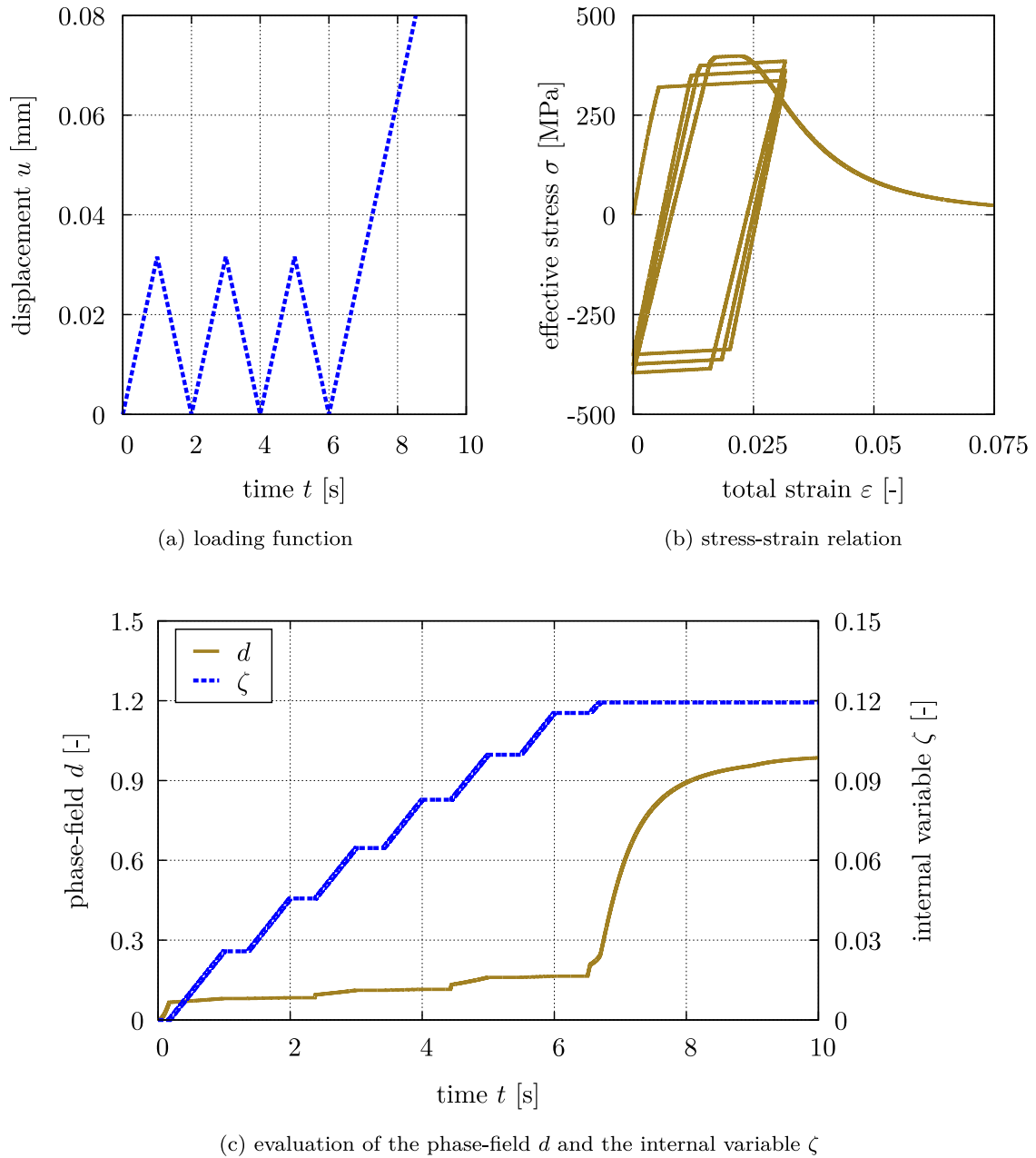
(a) loading function

(b) stress-strain relation

(c) evaluation of the phase-field d and the internal variable ζ

Fig. 5. Fracture evaluation by applying a cyclic loading, (a) definition of the displacement u with respect to the time t, (b) the stress–strain relationship and (c) the evaluation of the phase-field d and the equivalent plastic strain variable ζ.

cases. These simulations are performed as a quasi-static analysis and the solution scheme is based on a staggered method.

The location of the crack initiation and the final crack profile regarding different finite element discretizations are investigated and evaluated. By applying the presented ductile phase-field fracture, the phase-field crack starts to evolve in the vicinity of zones, where the maximum plastic deformation is concentrated. In the sequel, the crack searches for the next maximum plastic deformation to propagate at a new damaged profile. Based on the resolution of the FE discretizations, a significant difference for the position of crack initiation is observed, see Fig. 7(a)–(c) for tension failure and Fig. 9(a)–(c) for compression failure. Regarding a coarse mesh, the plastic deformation is
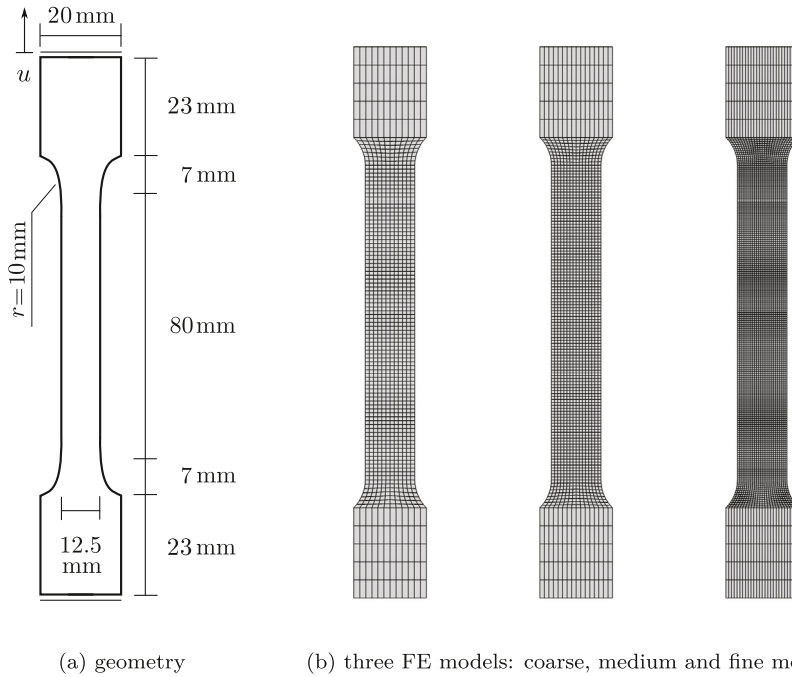
(a) geometry

(b) three FE models: coarse, medium and fine meshes

Fig. 6. Two-dimensional I-shaped structure test, (a) the geometric setup and (b) three different FE discretizations.

(a) coarse mesh (b) medium mesh (c) fine mesh

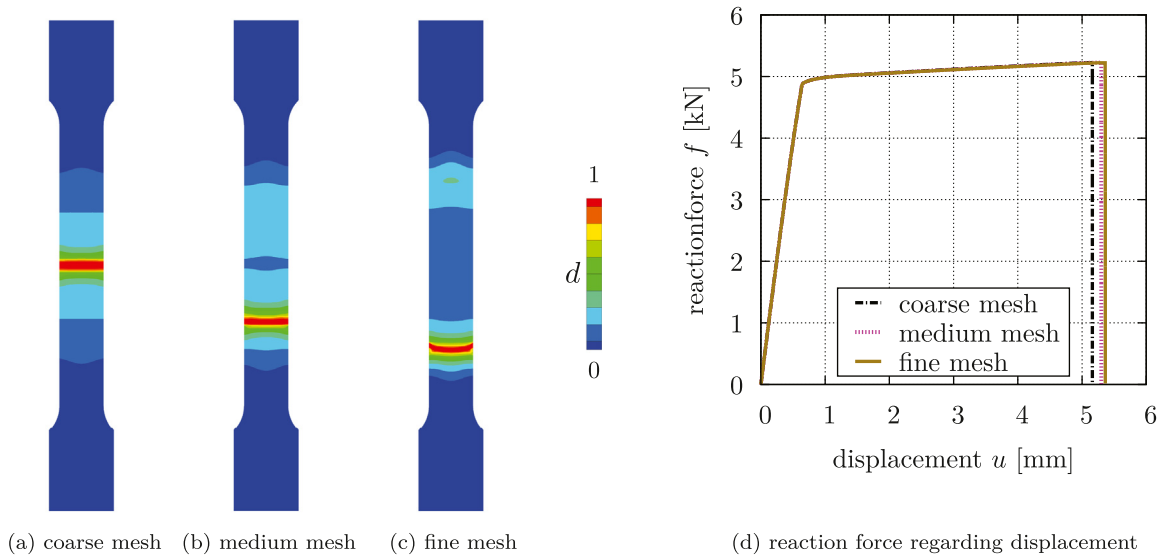(d) reaction force regarding displacement

Fig. 7. Tension failure regarding different FE discretizations (a)–(c) and (d) the relation between the reaction force and the displacement.

relatively uniform throughout the slender part of the specimen and fracture initiation approximately evolves at the middle of the specimen and propagates from center outwards to two edges. The consequent crack pattern also depends on the loading condition, i.e. the phase-field crack is close to a straight line for tension fracture and is inclined to 45 degrees for compression fracture. The key reason of such phenomena is the classical volumetric–deviatoric split for the phase-field model. The simulation results by the medium and fine meshes show different concentrations of the plastic deformation initially, which is offset from the middle part of the specimen. As a result, the phase-field profiles differ from each other, that shows a mesh dependency property due to classical
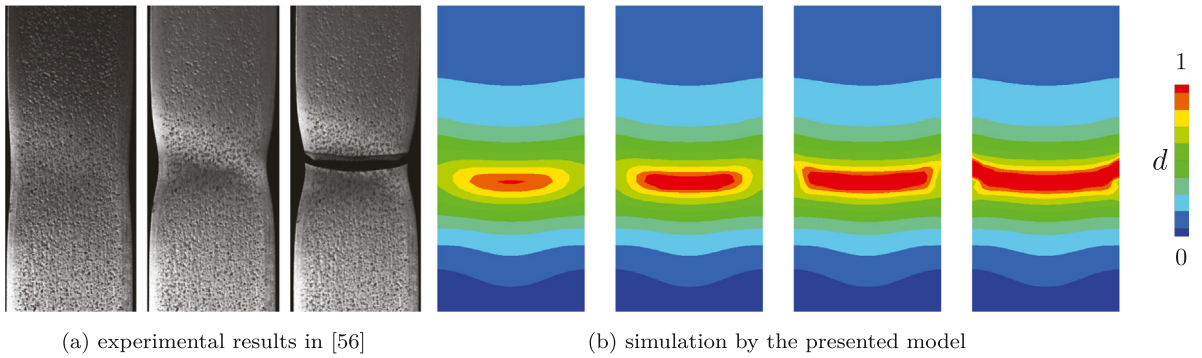
(a) experimental results in [56]   (b) simulation by the presented model

Fig. 8. Comparison of (a) the experimental validation of a ductile fracture in [56] and (b) the simulation results of the fine mesh model by the presented ductile phase-field formulation.
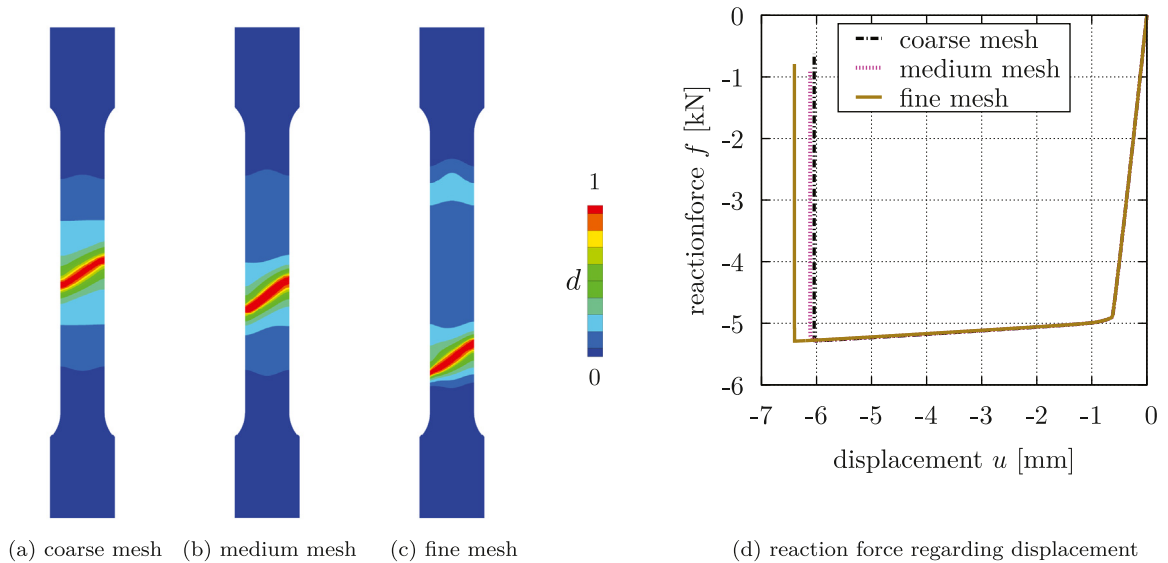

(a) coarse mesh   (b) medium mesh   (c) fine mesh   (d) reaction force regarding displacement

Fig. 9. Compression failure regarding different FE discretizations (a)–(c) and (d) the relation between the reaction force and the displacement.

plasticity theory. This phenomenon has been particularly discussed in [65] by comparing the phase-field approach and the microplane damage method for ductile fracture. Moreover, the crack path obtained by a fine mesh model shows a first straight crack and a subsequent inclined crack path near two edges, see Fig. 8(b) for a detailed view. Good agreement is observed by comparing the experimental validation in [56]. Furthermore, the reaction forces for the three meshes with respect to the tension and compression failure are compared in Fig. 7(d) and Fig. 9(d), respectively. The reaction force for compression failure does not eventually converge to 0 kN, since the volumetric contribution is circumvented to be degraded in a compression state based on the volumetric–deviatoric split.

4.3. Ductile fracture of a specimen with symmetrical hole-notches

In this example, in order to examine crack initiation depending on notch radii [66], the benchmark test by AMBATI et al. [55] is reproduced with the presented ductile phase-field formulation. A two-dimensional boundary value problem with symmetrical hole-notches is subjected to a tension load at the upper edge, while the lower edge is completely fixed. Two geometries are considered with regard to different radii $r = [2.5, 5]$ mm for the hole-notches, which are depicted in Figs. 10(a) and 11(a), respectively. The model parameters are listed in Table 3 and two scaling factors $a = [0.4, 0.5]$ are applied to govern the ductile phase-field evolution. Two different numerical discretizations

Table 3
Model parameters for the symmetrically notched specimens.

Bulk modulus κ	71 660 MPa	Fracture toughness $\mathcal{G}_c^0$	$95 \cdot e^3$ kJ/m^2
Shear modulus μ	27 280 MPa	Critical value ζ_{cr}	0.02
Hardening modulus H	250 MPa	Factor b	$1 \cdot e^{-8}$
Yielding stress σ_y	345 MPa	Length scale l	0.3 mm

(a) geometry   (b) the phase-field evolution   (c) load-displacement relations
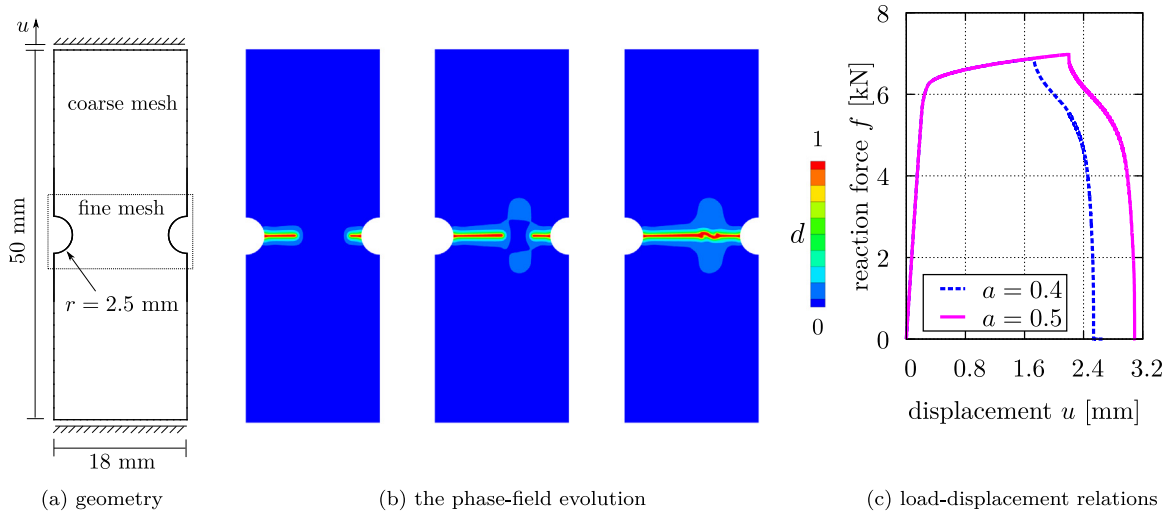
Fig. 10. Simulation results of the specimen for $r = 2.5$ mm, (a) geometric setup and loading conditions, (b) predicted crack path approximated by the phase-field evolution for $a = 0.4$ and (c) relationship between the reaction force f and the displacement u regarding different factors $a = [0.4, 0.5]$.
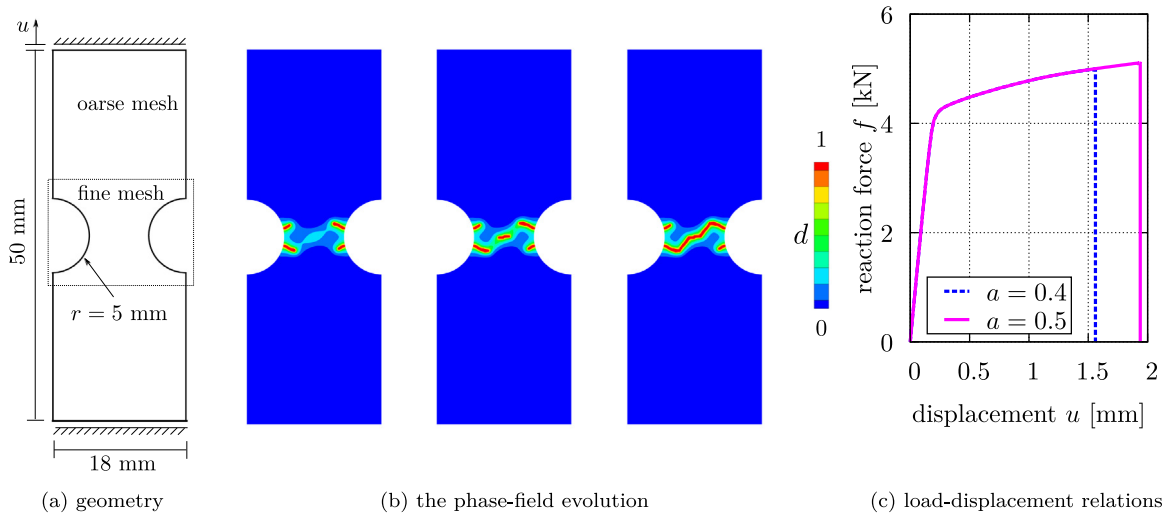

(a) geometry   (b) the phase-field evolution   (c) load-displacement relations

Fig. 11. Simulation results of the specimen for $r = 5$ mm, (a) geometric setup and loading conditions, (b) the predicted crack path approximated by the phase-field evolution for $a = 0.4$ and (c) relationship between the reaction force f and the displacement u regarding different factors $a = [0.4, 0.5]$.

regarding the geometries with radii $r = [2.5, 5]$ mm are taken into account, which consist of 12 860 and 11 200 4-node quadratic linear elements, respectively. To improve the computational efficiency, only the potentially cracked
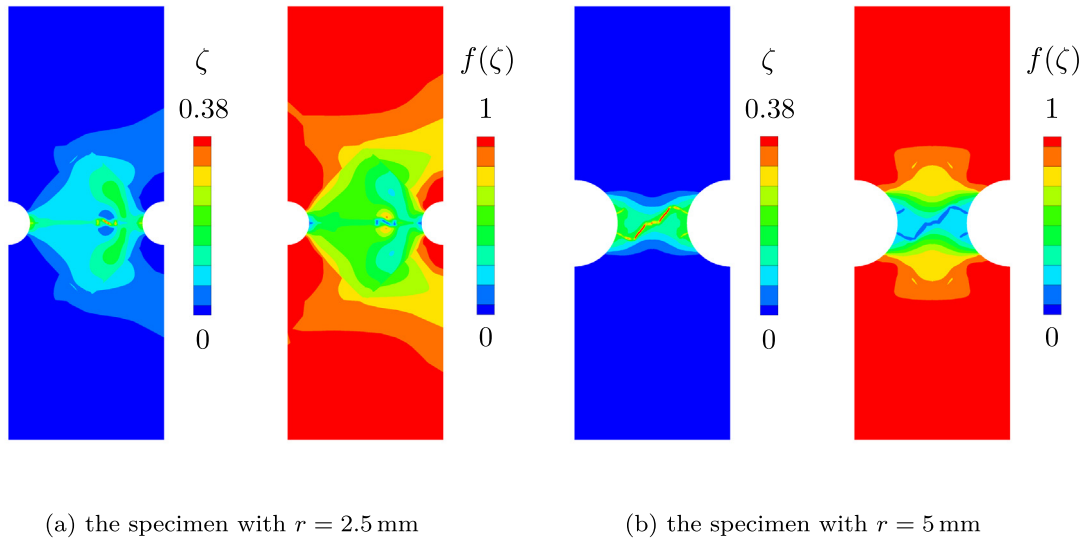
(a) the specimen with $r = 2.5\,\mathrm{mm}$ (b) the specimen with $r = 5\,\mathrm{mm}$

Fig. 12. The contour plot of the equivalent plastic strain ζ and the hardening degradation function $f(\zeta)$ for both simulations of $r = 2.5$ mm (a) and $r = 5$ mm (b) at fully cracked states by applying $a = 0.4$.

region is discretized by fine meshes with the element size of 0.07 mm $\leq h_e \leq$ 0.09 mm for the two geometries. These simulations are performed as quasi-static analysis and the solution scheme is based on a staggered method.

The phase-field evolution regarding the model with $r = 2.5$ mm is shown in Fig. 10(b) at three different loading status. It can be clearly observed that two cracks initiate at the middle of the curved notches. In the sequel, the cracks propagate inwards to the center of the specimen unsymmetrically up to the eventual failure. The loading–displacement relation is also measured regarding two scaling factors a in Fig. 10(c). For the geometry setup of $r = 5$ mm, two cracks initiate at the positions offset to the middle of the notches, meanwhile, an internal crack forms at the center of the specimen. Subsequently, the cracks merge together to form an unsymmetric and thorough crack path, which approximately follows the shear bands at an angle of 45 degrees to the loading direction, see Fig. 11(b). Correspondingly, the load–displacement curves are measured as well in Fig. 11(c). Furthermore, the distribution of the equivalent plastic strain ζ and the degradation function $f(\zeta)$ are shown in Figs. 12(a) and (b) regarding the complete fracture state of the model with $r = 2.5$ mm and the model with $r = 5$ mm, respectively.

Since the maximum equivalent plastic strain concentrates at different positions depending on the geometric setup, the initiation and merging of the cracks show obvious dissimilarities by considering these two notch radii. Meanwhile, the profiles of the load–displacement curves regarding different geometric setups also show differences. An abrupt failure is observed for the specimen with the larger notches, nevertheless, the smaller notched specimen yields a smooth softening behavior before the abrupt failure. Comparing these simulation results to [55], both the predicted crack paths and the profiles of the loading–displacement relations show thorough agreement.

Moreover, the numerical convergence for the staggered solution scheme is studied as well. The convergence criteria of the multi-field problem for the staggered solution are generally based on the numerical convergence of the decoupled equilibriums, which requires both the mechanical equilibrium and the ductile phase-field evolution to achieve converged states simultaneously at every loading step. Therefore, these two equilibriums are necessarily solved in an iterative manner, see [55] for the detailed algorithmic description. This approach leads to trustful simulation results compared to experiment data, nonetheless, it significantly decreases the computational efficiency and increases the simulation time. Therefore, a simplified staggered loop is sometimes also used, which only solves the mechanical response and the phase-field evolution once at each loading step. As a result, the simulation results are always overestimated compared to the experiment results as well as to the iterative staggered solution. In this work, taking the advantages of both staggered schemes, the simulation starts with the simplified staggered solution up to $d \leq 0.1$ and, subsequently, activates the iterative staggered solution as soon as $d > 0.1$ until final fracture. Taking the simulation of $r = 2.5$ mm and $a = 0.4$ as an example, the numerical convergence is evaluated. When applying the simplified staggered method, the mechanical solution regarding elasto-plasticity shows a promising
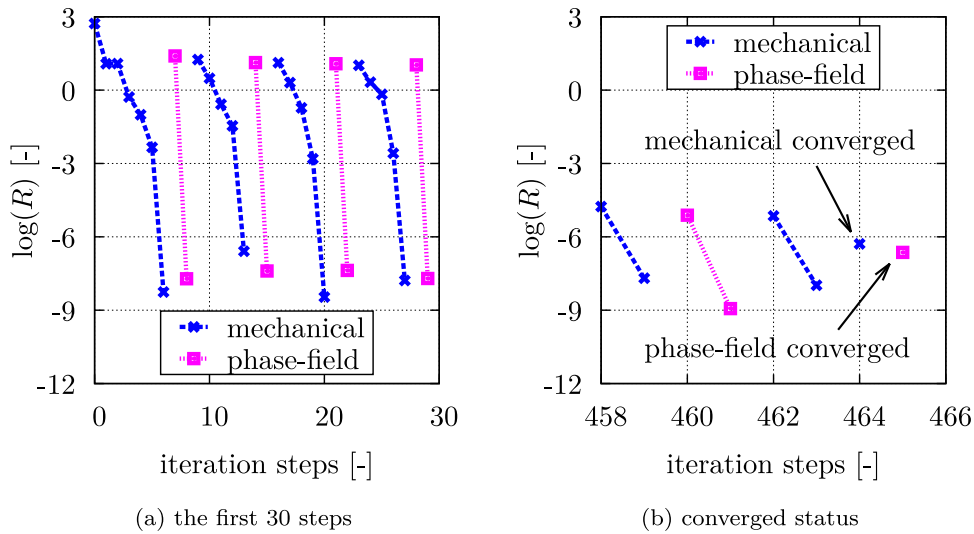
(a) the first 30 steps   (b) converged status

Fig. 13. Convergence of the staggered solution scheme at one loading step for $r = 2.5$ mm and $a = 0.4$, iterations for the first 30 steps in (a) and finally for multi-field converged status in (b) by investigating the logarithmic value of the residual norms $\log(\|\boldsymbol{R_u}\|)$ and $\log(\|\boldsymbol{R_d}\|)$.
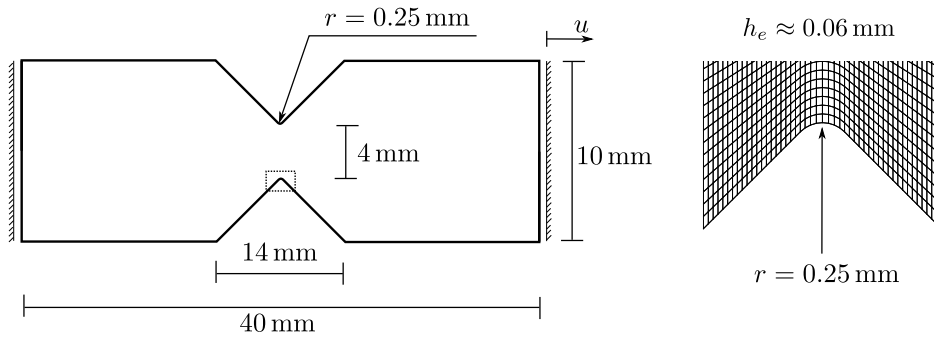

Fig. 14. Geometry setup and boundary condition of the two-dimensional V-notch specimen.

quadratic convergence and the phase-field solution only requires two steps to reach a converged state at each step. In the sequel, when $d > 0.1$, the iterative staggered strategy is considered, which naturally slows down the simulation. Before the phase-field crack is initiated, when $d \leq 0.9$, only a few iterations between the decoupled equilibriums are required. Nonetheless, the iteration steps are significantly increased when the phase-field crack initiates or propagates. Fig. 13 has demonstrated the iteration steps for both equilibriums at one loading step when the crack is propagating. The logarithmic value of the numerical residuals of both the mechanical field and the phase-field is recorded. Since the amount of iteration steps is large, only the first 30 steps and the consequently converged status are shown in Fig. 13(a) and (b), respectively. Furthermore, it is necessary to point out that, due to an extremely slight difference of the floating numbers stored in the solution arrays, the iterative staggered method possibly leads to an unsymmetric solution even dealing with a symmetric problem.

4.4. Ductile fracture of a V-notch specimen in tension

This example is experimentally investigated by LI et al. [67] regarding ductile fracture of an Al-alloy (Al-6061) V-notch specimen. Subsequently, it is also numerically studied by MIEHE et al. [51] to apply the ductile phase-field model coupled with gradient-enhanced plasticity. In this work, this example is reproduced by the presented ductile phase-field model to demonstrate the applicability. The geometric setup of the two-dimensional boundary value problem is depicted in Fig. 14 and the material parameters are given in Table 4. The finite element model of the

Table 4
Model parameters for the V-notch specimen test.

Bulk modulus κ	67 549 MPa	Fracture toughness $\mathcal{G}_c^0$	90 J/mm^2
Shear modulus μ	25 902 MPa	Factor b	$1 \cdot e^{-8}$
Hardening modulus H	561 MPa	Critical value ζ_{cr}	0
Yielding stress σ_y	475 MPa	Length scale l	0.2 mm

(a) The phase-field evolution   (b) load-displacement relations
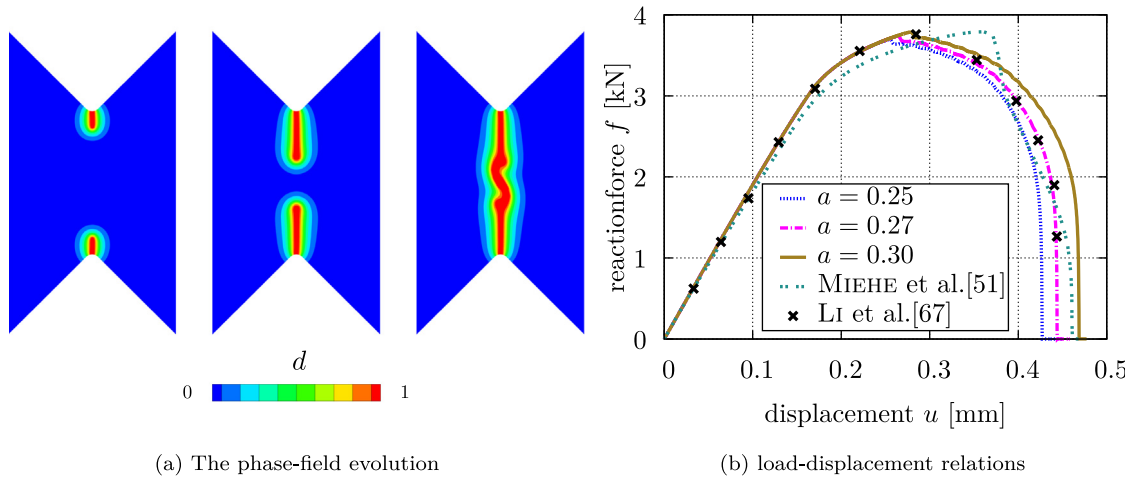
Fig. 15. Simulation results of the V-notch specimen by the presented ductile phase-field model, (a) phase-field evolution in the V-notch specimen for $a = 0.27$ and (b) comparison of the reaction forces of the presented model, the model proposed by MIEHE et al. [51] and the experimental investigation by LI et al. [67].

specimen is discretized by 11 680 4-node linear quadratic elements and the element size at the potential crack region is $h_e \approx 0.06$ mm.

The simulation is performed by applying a set of factors $a = [0.25, 0.27, 0.3]$ to appropriately capture the experimental data in [67]. The relations between the load and displacement obtained by the presented model are compared to the results of [51,67] in Fig. 15(b), which show good agreement to each other. Particularly, the phase-field evolution of the specimen by applying $a = 0.27$ is shown in Fig. 15(a). The crack initiates at the tip of the curved notch where the maximum equivalent plastic strain ζ develops. Then, it stably propagates from the notches inwards up to the final rupture with a curved crack path. Explained in [51], the predicted crack path is not straight and not perpendicular to the loading direction due to the characteristics of the simple VON MISES plasticity. Furthermore, the evolution of the equivalent plastic strain ζ and the degradation function $f(\zeta)$ with respect to the corresponding phase-field states in Fig. 15(a) are shown in Fig. 16 as well.

4.5. Ductile fracture of an SHCC-dogbone structure

In this example, the fracture properties of *Strain Hardening Cement-based Composites (SHCC)* are studied. As a recently developed composite material, SHCC consists of a finely grained cementitious matrix and high-performance polymeric fibers, which are short and randomly orientated. A detailed description of SHCC's material properties and applications is referred to [68]. In this work, a three-dimensional dogbone structure is analyzed to investigate the fracture behavior, where the geometric and experimental setups are depicted in Fig. 17(a) and (b), respectively. SHCC is characterized as an anisotropic and heterogeneous material due to the appearance of micro voids and reinforcing fibers in the cement matrix. Nevertheless, in order to simplify the problem and to achieve an effective investigation of the fracture mechanism, the dogbone structure is assumed to be homogeneous and to exhibit isotropic behavior.

Outlined in [68], as soon as the micro cracks inside the structure are formed, the fibers bridging the two crack surfaces can still transfer a portion of tensile loading and maintain the structural integrity. By increasing external
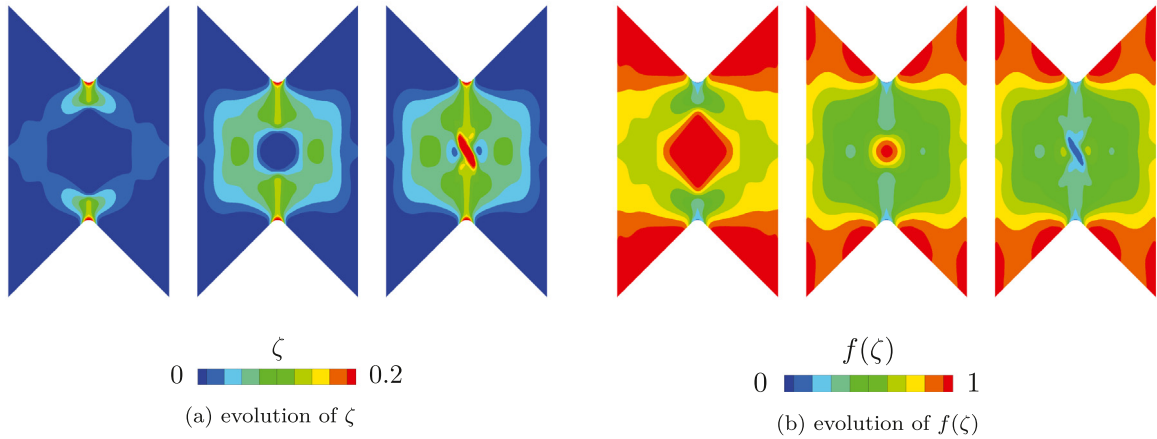
ζ

0 ▮▮▮▮▮▮▮▮ 0.2

(a) evolution of ζ

$f(\zeta)$

0 ▮▮▮▮▮▮▮▮ 1

(b) evolution of $f(\zeta)$

Fig. 16. Evolution of the equivalent plastic strain ζ (a) and the degradation function $f(\zeta)$ (b) regarding the phase-field states in Fig. 15(a), respectively.
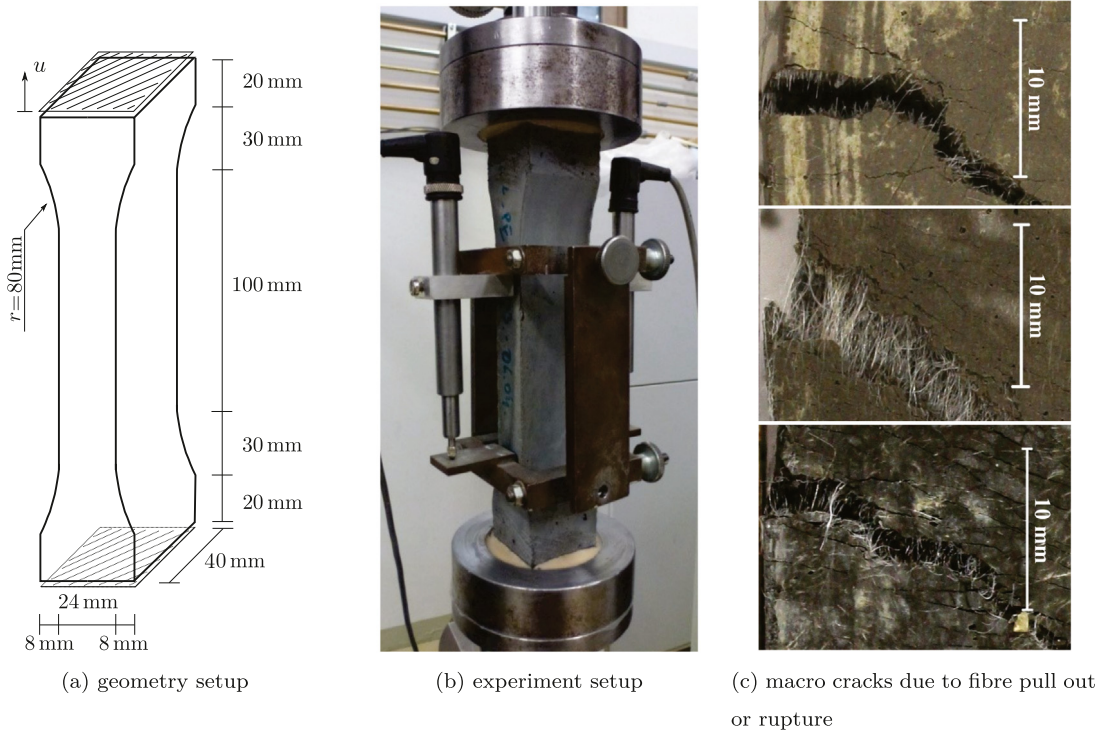

(a) geometry setup

(b) experiment setup

(c) macro cracks due to fibre pull out or rupture

Fig. 17. Tension test of SHCC-dogbone specimen, (a) geometry of the specimen, (b) experiment setup outlined in [68] and (c) a detailed investigation of cracks in the cement matrix including the bridging fibers regarding different types of SHCC, see [68].

loads, further micro cracks initiate and merge to form visible macro cracks until the final structural failure governed by either fiber pull out or rupture, see Fig. 17(c). The overall stress–strain relationship shows an initial linear elastic stage before the formation of the first crack in the matrix. In the sequel, the stress keeps an increasing trend with oscillations due to newly formed cracks up to final failure. These characteristics can be alternatively explained by the concept of ductile fracture from the macro scale point of view. The study [65] successfully investigates the fracture evolution of the SHCC dogbone structure by applying the ductile phase-field formulation proposed in [55].
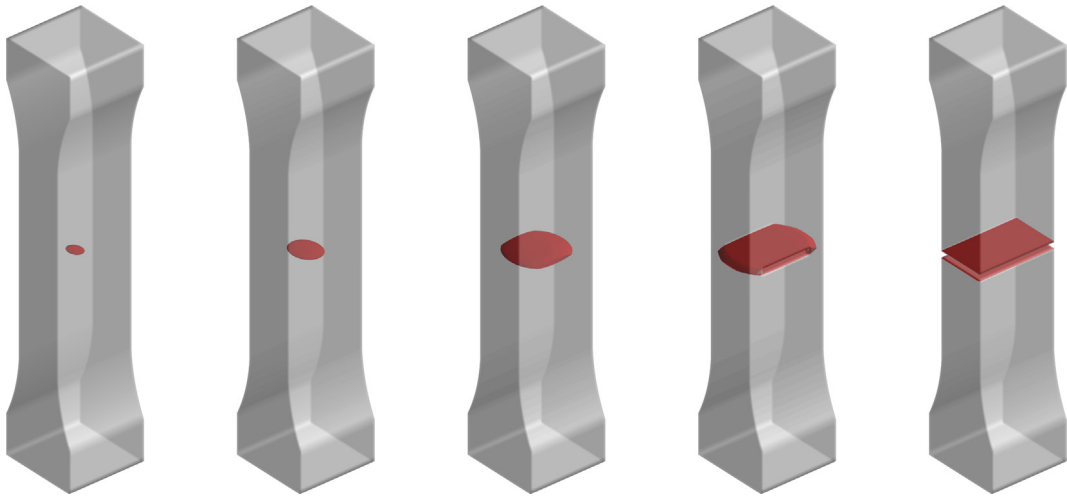
Fig. 18. Fracture evolution of the SHCC-dogbone specimen for $a = 0.1$, crack initiating in the center of the specimen and propagating outwards to the edges, phase-field crack surface shown by plotting the isosurface of $d = 0.95$ and blanking the values $d > 0.95$.

Table 5

Model parameters for the SHCC dogbone specimen test.

Bulk modulus κ	17 778 MPa	Fracture toughness $\mathcal{G}_c^0$	18 J/mm^2
Shear modulus μ	13 333 MPa	Factor b	$1 \cdot e^{-8}$
Hardening modulus H	167 MPa	Critical value ζ_{cr}	0.01
Yielding stress σ_y	2.26 MPa	Length scale l	4 mm

In this work, ductile failure of SHCC is simulated and the results are compared to the experiments in [68] in order to demonstrate the capability of the presented phase-field model.

The specimen is subjected to tensile loading by clamping the top and bottom surfaces. The numerical model is uniformly discretized by 57 344 8-node linear brick elements with the size of $h_e = 1.5$ mm. As stated in [68], the loading rate has a strong influence on the material property. The material constants for the numerical simulation are identified at the strain rate of $\dot{\varepsilon} = 2 \cdot e^{-4}$ s^{-1}, which are listed in Table 5. Several scaling factors $a = [0.065, 0.1, 0.2]$ are tested to properly capture the fracture response conducted in [68]. The phase-field crack evolution regarding $a = 0.1$ is shown in Fig. 18. The crack initiates at the center of the cross-section and propagates outwards to the edges. Since the FE model is discretized by relatively coarse meshes, the crack pattern shows more or less a plane instead of a curved surface, which has been particularly discussed in Section 4.2. Similar simulations can be found in [56] and [65], that also show a consequent straight plane crack in a three-dimensional geometry with coarse mesh. The stress–strain relationships regarding different scaling factors a are compared to the experiment in Fig. 19, where good agreement is obtained by applying the scaling factor $a = 0.1$.

5. Conclusions

Phase-field modeling has become a promising approach to simulate GRIFFITH-type brittle fracture. In this paper, a ductile phase-field formulation coupled to classical VON MISES plasticity is postulated by defining the fracture toughness $\mathcal{G}_c$ as a quantity depending upon the accumulative equivalent plastic strain. The presented phase-field model strictly follows the definition of GRIFFITH-type fracture, that defines the fracture driving force only consisting of the pure elastic strain energy. The consequent governing equation for the phase-field contains two degradation functions $g(d)$ and $f(\zeta)$, which are multiplied to the fracture driving force $\mathcal{H}$ and the fracture toughness $\mathcal{G}_c^0$, respectively. Furthermore, an important assumption of $\partial f(\zeta) / \partial \zeta = 0$ largely simplifies the derivation and recovers a standard plasticity evolution law regarding the mechanical equilibrium. Meanwhile, this newly developed ductile phase-field model is formulated and implemented within the small strain framework, nevertheless, it can be straightforwardly extended to finite strains.
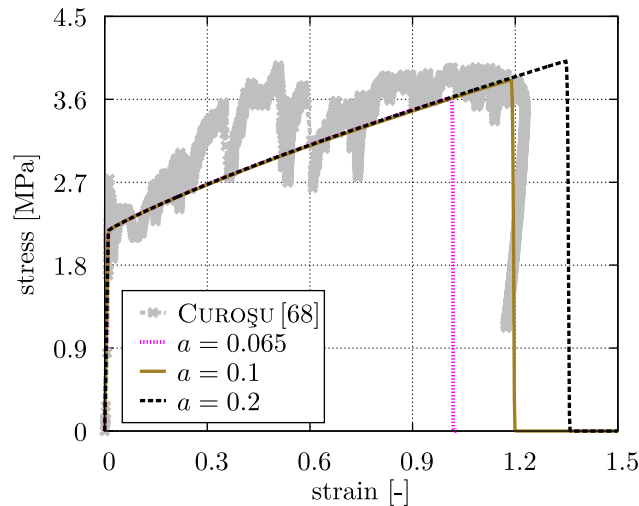
Fig. 19. Comparison of the stress and strain relationship obtained by presented model and the experimental investigation by CUROȘU in [68].

A variety of aforementioned phase-field models have been proposed for ductile fracture, which are generally classified into two categories. The first one re-defines the fracture driving force, which consists of the elastic energy and the pseudo plastic energy, see e.g. [45–47], just to name a few. The pseudo plastic energy is characterized as a sort of dissipative energy due to inelasticity and it is difficult to physically and straightforwardly explain how the dissipated plastic energy evolves the fracture. The second category of ductile phase-field model modifies the degradation function $g(d)$, see [55,56], which strictly follows the GRIFFITH-type fracture definition. Nevertheless, due to $g(d)$ depending on ζ, the linearity of the phase-field evolution is lost and an additional numerical perturbation is required. Compared to the existing models, the novelty of the presented model is, that it strictly follows GRIFFITH-type fracture definition and does not change the linearity of the phase-field governing equation. Changing of the material property due to plastic deformations, e.g. the degradation of $\mathcal{G}_c^0$, can be physically explained from the micro-structure point of view. Similar approaches are referred to [58–61]. Meanwhile, several convincing examples are obtained, that show good agreements with other numerical benchmarks as well as experimentally predictions, e.g. [47,51,55,64–68].

The introduced method is not only restricted to the small strain framework, whereas the extension to finite strain is the next priority. As an open topic, alternative definitions of $f(\zeta)$ can be further studied by incorporating a multi-scale approach. Furthermore, based on experimental evidence, the property of rate-dependent ductile fracture is also an attractive focus for future work.

Declaration of competing interest

The authors declare that they have no known competing financial interests or personal relationships that could have appeared to influence the work reported in this paper.

Acknowledgments

References

[1] A.A. Griffith, The phenomena of rupture and flow in solids, Philos. Trans. R. Soc. Lond. Ser. A 221 (1921) 163–198.
[2] J.C. Simo, T.J.R. Hughes, Computational Inelasticity, Springer, New York, 1998.
[3] J. Lemaitre, J. Chaboche, Mechanics of Solid Materials, Cambridge University Press, Cambridge, 1990.
[4] J. Besson, Continuum models of ductile fracture: a review, Int. J. Damage Mech. 19 (2010) 3–52.

[5] G. Johnson, W. Cook, Fracture characteristics of three metals subjected to various strains, strain rates, temperatures and pressures, Eng. Fract. Mech. 21 (1985) 31–48.

[6] J. Lemaitre, A continuous damage mechanics model for ductile fracture, J. Eng. Mater. Technol. 107 (1985) 83–89.

[7] R. De Borst, J. Pamin, M.G.D. Geers, On coupled gradient-dependent plasticity and damage theories with a view to localization analysis, Eur. J. Mech. A Solids 18 (1999) 939–962.

[8] B. Nedjar, Elastoplastic-damage modelling including the gradient of damage: formulation and computational aspects, Int. J. Solids Struct. 38 (2001) 5421–5451.

[9] F. Reusch, B. Svendsen, D. Klingbeil, Local and non-local gurson-based ductile damage and failure modelling at large deformation, Eur. J. Mech. A Solids 22 (2003) 779–792.

[10] M. Jirásek, S. Rolshoven, Localization properties of strain-softening gradient plasticity models. Part I: Strain-gradient theories, Int. J. Solids Struct. 46 (2009) 2225–2238.

[11] L. Jason, A. Huerta, G. Pijaudier-Cabot, S. Ghavamian, An elastic plastic damage formulation for concrete: Application to elementary tests and comparison with an isotropic damage model, Comput. Methods Appl. Mech. Engrg. 195 (2006) 7077–7092.

[12] J. Lee, G.L. Fenves, Plastic-damage model for cyclic loading of concrete structures, J. Eng. Mech. 124 (1998) 892–900.

[13] J.Y. Wu, J. Li, R. Faria, An energy release rate-based plastic-damage model for concrete, Int. J. Solids Struct. 43 (2006) 583–612.

[14] D. Xenos, D. Grégoire, S. Morel, P. Grassl, Calibration of nonlocal models for tensile fracture in quasi-brittle heterogeneous materials, J. Mech. Phys. Solids 82 (2015) 48–60.

[15] R. Alessi, J.J. Marigo, S. Vidoli, Gradient damage models coupled with plasticity and nucleation of cohesive cracks, Arch. Ration. Mech. Anal. 214 (2014) 575–615.

[16] R. Alessi, J.J. Marigo, S. Vidoli, Gradient damage models coupled with plasticity: Variational formulation and main properties, Mech. Mater. 80 (2015) 351–367.

[17] G.Z. Voyiadjis, Z.N. Taqieddin, P.I. Kattan, Anisotropic damage-plasticity model for concrete, Int. J. Plast. 24 (2008) 1946–1965.

[18] I. Carol, M. Jirásek, Z. Bažant, A thermodynamically consistent approach to microplane theory. Part I. free energy and consistent microplane stresses, Int. J. Solids Struct. 38 (2001) 2921–2931.

[19] A. Qinami, I. Zreid, R. Fleischhauer, M. Kaliske, Modeling of impact on concrete plates by use of the microplane approach, Int. J. Non-Linear Mech. 80 (2015) 107–121.

[20] I. Zreid, M. Kaliske, A gradient enhanced plasticity-damage microplane model for concrete, Int. J. Non-Linear Mech. 62 (2018) 1239–1257.

[21] M.E. Gurtin, Configurational Forces as Basic Concepts of Continuum Physics, Springer, New York, 2000.

[22] R. Kienzler, G. Herrmann, Mechanics in Material Space: With Applications to Defect and Fracture Mechanics, Springer, Berlin, 2000.

[23] M. Braun, Configurational forces induced by finite-element discretization, Proc. Est. Acad. Sci. Phys. Math. 35 (1997) 379–386.

[24] R. Müller, G.A. Maugin, On material forces and finite element discretizations, Comput. Mech. 29 (2002) 52–60.

[25] G.A. Maugin, Material forces: Concepts and applications, Appl. Mech. Rev. 48 (1995) 213–245.

[26] G.A. Maugin, Configurational Forces: Thermomechanics, Physics, Mathematics, and Numerics, CRC Press, Boca Raton, 2010.

[27] J.W. Foulk, D.H. Allen, K.L.E. Helms, Formulation of a three-dimensional cohesive zone model for application to a finite element algorithm, Comput. Methods Appl. Mech. Engrg. 183 (2000) 51–66.

[28] G.A. Francfort, J.J. Marigo, Revisiting brittle fracture as an energy minimization problem, J. Mech. Phys. Solids 46 (1998) 1319–1342.

[29] B. Bourdin, G.A. Francfort, J.J. Marigo, Numerical experiments in revisited brittle fracture, J. Mech. Phys. Solids 48 (2000) 797–826.

[30] V. Hakim, A. Karma, Laws of crack motion and phase-field models of fracture, J. Mech. Phys. Solids 57 (2009) 342–368.

[31] C. Miehe, F. Welschinger, M. Hofacker, Thermodynamically consistent phase-field models of fracture: Variational principles and multi-field FE implementations, Int. J. Numer. Methods Eng. 83 (2010) 1273–1311.

[32] K. Pham, H. Amor, J. Marigo, C. Maurini, Gradient damage models and their use to approximate brittle fracture, Int. J. Damage Mech. 20 (2011) 618–652.

[33] D. Mumford, J. Shah, Optimal approximations by piecewise smooth functions and associated variational problems, Comm. Pure Appl. Math. 42 (1989) 577–685.

[34] L. Ambrosio, V.M. Tortorelli, Approximation of functionals depending on jumps by elliptic functionals via convergence, Comm. Pure Appl. Math. 43 (1990) 999–1036.

[35] G. Dal Maso, An Introduction to Γ-Convergence, Birkhäuser, Boston, 1993.

[36] D.P. Braides, Approximation of Free Discontinuity Problems, Springer, Berlin, 1998.

[37] A. Braides, Gamma-Convergence for Beginners, Oxford University Press, Oxford, 2002.

[38] M.J. Borden, T.J.R. Hughes, C.M. Landis, C.V. Verhoosel, A higher-order phase-field model for brittle fracture: Formulation and analysis within the isogeometric analysis framework, Comput. Methods Appl. Mech. Engrg. 273 (2014) 100–118.

[39] H. Amor, J.J. Marigo, C. Maurini, Regularized formulation of the variational brittle fracture with unilateral contact: Numerical experiments, J. Mech. Phys. Solids 57 (2009) 1209–1229.

[40] C. Miehe, M. Hofacker, F. Welschinger, A phase field model for rate-independent crack propagation: Robust algorithmic implementation based on operator splits, Comput. Methods Appl. Mech. Engrg. 199 (2010) 2765–2778.

[41] M. Hofacker, A Thermodynamically Consistent Phase Field Approach to Fracture (Ph.D. thesis), Universität Stuttgart, 2013.

[42] C. Steinke, M. Kaliske, A phase-field crack model based on directional stress decomposition, Comput. Mech. 63 (2019) 1019–1046.

[43] J. Storm, D. Supriatna, M. Kaliske, The concept of Representative Crack Elements (RCE) for phase-field fracture - Anisotropic elasticity and thermo-elasticity, Int. J. Numer. Methods Eng. http://dx.doi.org/10.1002/nme.6244.

[44] F.P. Duda, A. Ciarbonetti, P.J. Sánchez, A.E. Huespe, A phase-field/gradient damage model for brittle fracture in elastic–plastic solids, Int. J. Plast. 65 (2015) 269–296.

[45] C. Miehe, M. Hofacker, L. Schänzel, F. Aldakheel, Phase field modeling of fracture in multi-physics problems. part II. coupled brittle-to-ductile failure criteria and crack propagation in thermo-elastic–plastic solids, Comput. Methods Appl. Mech. Engrg. 294 (2015) 486–522.

[46] C. Kuhn, T. Noll, R. Müller, On phase field modeling of ductile fracture, Surv. Appl. Math. Mech. 39 (2016) 35–54.

[47] M.J. Borden, T.J.R. Hughes, C.M. Landis, A. Anvari, I.J. Lee, A phase-field formulation for fracture in ductile materials: Finite deformation balance law derivation, plastic degradation, and stress triaxiality effects, Comput. Methods Appl. Mech. Engrg. 312 (2016) 130–166.

[48] D. Kienle, F. Aldakheel, M.A. Keip, A finite-strain phase-field approach to ductile failure of frictional materials, Int. J. Solids Struct. 172–173 (2019) 147–162.

[49] R. Alessi, J.J. Marigo, C. Maurini, S. Vidoli, Coupling damage and plasticity for a phase-field regularisation of brittle, cohesive and ductile fracture: One-dimensional examples, Int. J. Mech. Sci. 149 (2018) 559–576.

[50] C. Miehe, S. Teichtmeister, F. Aldakheel, Phase-field modelling of ductile fracture: a variational gradient-extended plasticity-damage theory and its micromorphic regularization, Phil. Trans. R. Soc. A 374 (2016).

[51] C. Miehe, F. Aldakheel, A. Raina, Phase field modeling of ductile fracture at finite strains. a variational gradient-extended plasticity-damage theory, Int. J. Plast. 84 (2016) 1–32.

[52] F. Aldakheel, Mechanics of Nonlocal Dissipative Solids: Gradient Plasticity and Phase Field Modeling of Ductile Fracture (Ph.D. thesis), Stuttgart Universität, 2016.

[53] C. Miehe, D. Kienle, F. Aldakheel, S. Teichtmeister, Phase field modeling of fracture in porous plasticity: A variational gradient-extended eulerian framework for the macroscopic analysis of ductile failure, Comput. Methods Appl. Mech. Engrg. 312 (2016) 3–50.

[54] F. Aldakheel, P. Wriggers, C. Miehe, A modified Gurson-type plasticity model at finite strains: formulation, numerical analysis and phase-field coupling, Comput. Mech. 62 (2018) 815–833.

[55] M. Ambati, T. Gerasimov, L. De Lorenzis, Phase-field modeling of ductile fracture, Comput. Mech. 55 (2015) 1017–1040.

[56] M. Ambati, R. Kruse, L. De Lorenzis, A phase-field model for ductile fracture at finite strains and its experimental verification, Comput. Mech. 57 (2016) 149–167.

[57] R. Alessi, M. Ambati, T. Gerasimov, S. Vidoli, L. De Lorenzis, Comparison of phase-field models of fracture coupled with plasticity, Comput. Methods Appl. Sci. (2018) http://dx.doi.org/10.1007/978-3-319-60885-3_1.

[58] R. Alessi, S. Vidoli, L. De Lorenzis, A phenomenological approach to fatigue with a variational phase-field model: The one-dimensional case, Eng. Fract. Mech. 190 (2018) 53–73.

[59] P. Carrara, M. Ambati, R. Alessi, L. De Lorenzis, A framework to model the fatigue behavior of brittle materials based on a variational phase-field approach, Comput. Methods Appl. Mech. Engrg. (2019) http://dx.doi.org/10.1016/j.cma.2019.112731.

[60] M. Seiler, T. Linse, P. Hantschke, M. Kästner, An efficient phase-field model for fatigue fracture in ductile materials, Eng. Fract. Mech. (2019) http://dx.doi.org/10.1016/j.engfracmech.2019.106807.

[61] B. Yin, C. Steinke, M. Kaliske, Formulation and implementation of strain rate dependent fracture toughness in context of the phase-field method, Internat. J. Numer. Methods Engrg. 121 (2020) 233–255.

[62] B. Yin, M. Kaliske, Fracture simulation of viscoelastic polymers by the phase-field method, Comput. Mech. http://dx.doi.org/10.1007/s00466-019-01769-1.

[63] C. Kuhn, A. Schlüter, R. Müller, On degradation functions in phase field fracture models, Comput. Mater. Sci. 108 (2015) 374–384.

[64] M.J. Borden, Isogeometric Analysis of Phase-Field Models for Dynamic Brittle and Ductile Fracture (Ph.D. thesis), The University of Texas at Austin, 2012.

[65] C. Steinke, I. Zreid, M. Kaliske, Modelling of ductile fracture of strain-hardening cement-based composites-novel approaches based on microplane and phase-field method, in: Plasticity, Damage & Fracture in Advanced Materials, Springer, Berlin, 2019.

[66] M. Alves, N. Jones, Influence of hydrostatic stress on failure of axisymmetric notched specimens, J. Mech. Phys. Solids 47 (1997) 643–667.

[67] H. Li, M.W. Fu, J. Lu, H. Yang, Ductile fracture: Experiments and computations, Int. J. Plast. 27 (2011) 147–180.

[68] I. Curoşu, Influence of Fiber Type and Matrix Composition on the Tensile Behavior of Strain-Hardening Cement-Based Composites (SHCC) under Impact Loading (Ph.D. thesis), Technische Universität Dresden, 2017.